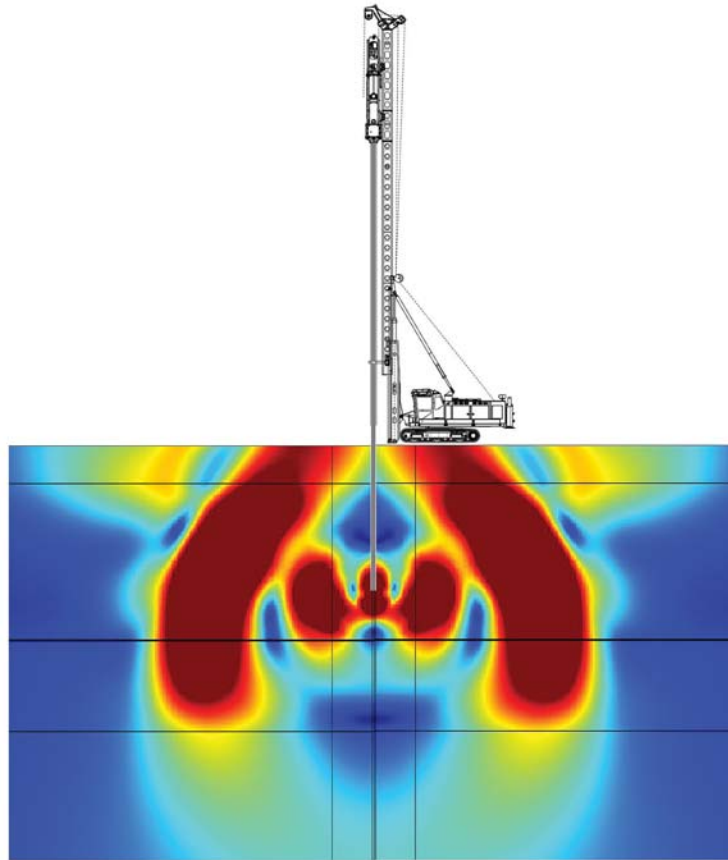




LUND  
UNIVERSITY



# NUMERICAL ANALYSIS OF VIBRATIONS DUE TO IMPACT PILE DRIVING

SEBASTIAN ANDERSSON OLIVECRONA  
and RASMUS SULANDER

Geotechnical  
Engineering

*Master's Dissertation*



DEPARTMENT OF CONSTRUCTION SCIENCES

## GEOTECHNICAL ENGINEERING

ISRN LUTVDG/TVGT--16/5058--SE (1-78) | ISSN 0349-4977

MASTER'S DISSERTATION

# NUMERICAL ANALYSIS OF VIBRATIONS DUE TO IMPACT PILE DRIVING

SEBASTIAN ANDERSSON OLIVECRONA  
and RASMUS SULANDER

Supervisors: Prof. **OLA DAHLBLOM**, Dept. of Construction Sciences, LTH, Lund  
and **ALEX SPETZ**, MSc, Geotechnical Engineering, LTH, Lund.

Project Manager: **PÄR SANDBLAD**, Skanska Sverige AB.

Examiner: **ERIKA TUDISCO**, PhD, Geotechnical Engineering, LTH, Lund.

Copyright © 2016 Geotechnical Engineering,  
Dept. of Construction Sciences, Faculty of Engineering LTH, Lund University, Sweden.

Printed by Media-Tryck LU, Lund, Sweden, August 2016 (*PI*).

**For information, address:**

Geotechnical Engineering, Dept. of Construction Sciences,  
Faculty of Engineering LTH, Lund University, Box 118, SE-221 00 Lund, Sweden.

Homepage: [www.geoteknik.lth.se](http://www.geoteknik.lth.se)



# Abstract

Vibrations originating from constructional work can affect the nearby soil and structures. Depending on the properties of the vibrations, these can result in settlements in the soil and damages to existing structures. Along with blasting, impact pile driving is one of the greatest sources of vibrations on a construction site.

When installing a concrete pile with an impact hammer, a weight is dropped at the head of the pile repeatedly until the pile is located in a desired position. The mechanism of load transfer from pile to soil decides whether the pile should be grouped as a friction pile, cohesion pile or an end bearing pile. When the pile is installed in a granular soil the resistance force along the shaft of the pile depends on the horizontal stress and the angle of friction between the pile and the soil. While installing a pile in a cohesion soil, the adhesion between pile and soil cannot be utilised since the soil is remoulded during pile driving.

Important soil properties that affect the vibration propagation in the soil are density, Young's modulus, Poisson's ratio and the stress state of the soil. Volume changes in the soil can occur if the soil is exposed to vibrations. The magnitude of the volume change is dependent on the angle of dilatation and the initial porosity. The three most common types of waves that propagate through the soil are the pressure wave, the shear wave and the Rayleigh wave.

In this report, the vibrations of a single hammer blow at different pile depths are studied and compared with a field test. The object is to investigate the possibility to make a satisfactory finite element simulation of the vibrations due to pile driving. Two soil plasticity models are used along with a linear elastic model. The plastic models are the Mohr-Coulomb yield criterion and the Drucker-Prager yield criterion.

No significant discrepancies were found in the vibration velocities in the different material models. Although, small differences in vibrations occur with the plastic Drucker-Prager model in comparison with the elastic model. Results show that the Young's modulus for a soil is decisive for the behaviour and magnitude of the vibrations.

The conclusion is that the finite element method can be successfully used to predict wave propagation and vibrations due to impact pile driving, regardless of which of the three material models that are used in the computation. Predicting the waves and vibrations can be a useful tool for reducing noise, settlements, damage and unpleasantness associated with pile installations.

## Keywords

Soil mechanics, soil dynamics, ground vibrations, impact pile driving, concrete pile, finite element method, COMSOL Multiphysics



# Sammanfattning

Vibrationer som uppkommer vid byggarbeten kan påverka omkringliggande jord och konstruktioner. Beroende på vibrationernas egenskaper så kan dessa leda till sättningar i jorden vilket kan generera skador på befintliga byggnader och anläggningar. Tillsammans med explosionsarbeten är påslagning den största källan till vibrationer från en byggarbetsplats.

När en betongpåle installeras med hammarslagning innebär det att en vikt släpps på pålhuvudet upprepade gånger tills pålen befinner sig i en önskad position i marken. Kraftöverföringen mellan påle och jord bestämmer om pålen ska klassas som en friktionspåle, kohesionspåle eller spetsburen påle. När en påle installeras i en granulär jord är motståndet längs med påskaftet beroende av den horisontella spänningen och friktionsvinkeln mellan påle och jord. När en påle installeras i en kohesionsjord kan inte adhesionen mellan påle och jord användas då jorden omfördelas i samband med påldrivning.

Viktiga jordparametrar som påverkar vibrationsutbredningen är jorddensiteten, elasticitetsmodulen, Poissons tal och spänningsförhållandena i jorden. Volymändringar i jorden kan uppstå om jorden är utsatt för vibrationer. Storleken på volymändringen är beroende av dilatationsvinkeln och den initiala porositeten. De tre vanligaste typerna av vågutbredning i jord är tryckvågen, skjuvvågen och Rayleighvågen.

I det här examensarbetet studeras vibrationerna som uppkommer från ett enskilt hammarslag och jämförs med resultat från ett fälttest. Syftet är att undersöka möjligheten att på ett tillfredsställande sätt genomföra en finita elementsimulering av vibrationerna som uppkommer vid påslagning. Två plastiska modeller och en linjärelastisk modell används. De plastiska modellerna är Mohr-Coulombs brottkriterium och Drucker-Pragers brottkriterium.

Inga signifikanta skillnader återfanns hos vibrationshastigheterna mellan de olika materialmodellerna. Dock kunde små skillnader urskiljas i vibrationerna med den plastiska Drucker-Pragermodellen i jämförelse med den elastiska. Resultaten visar att Elasticitetsmodulen för en jord spelar en avgörande roll för beteendet och storleken hos vibrationerna.

Slutsatsen är att finita elementmetoden kan användas för att approximativt förutsäga vågutbredning och vibrationerna som uppkommer från påslagningen, oavsett vilken av de tre materialmodellerna som används vid beräkningarna. Att kunna förutspå vågor och vibrationer kan vara ett användbart verktyg för att reducera oljud, sättningar, skador och obehagligheter som är förknippade med påldrivning.

Jordmekanik, jorddynamik, markvibrationer, påslagning, betongpåle, finita elementmetoden, COMSOL Multiphysics.



# Acknowledgements

This master's dissertation represents the end of an era. The thesis was conducted at the Department of Construction Sciences at Faculty of Engineering LTH, Lund University, during the period of January to June 2016.

We would like to give warm thanks to our supervisors at the Department of Construction Sciences, Professor Ola Dahlblom and Doctoral candidate Alex Spetz, for their unhesitating will to make this ship reach its harbour. Their knowledge and their outstanding experience has brought a comforting guidance throughout this stormy sea that has been this master's dissertation.

We would also like to give special thanks to Dr Sven Liedberg at Skanska and Doctoral candidate Carl Wersäll at KTH for their kind will to help us and answering our questions regarding soil dynamics. We would also like to thank Pär Sandblad at Skanska and Rune Westin at Comsol support.

Finally we would like to give colossal cheesy thanks to (Mum and Dad) x 2.

Lund June, 2016

Rasmus Sulander & Sebastian Andersson Olivecrona



# Contents

- Abstract ..... ii
- Sammanfattning.....iv
- Acknowledgements .....vi
- Chapter 1 Introduction ..... 1
  - 1.1 Background..... 1
  - 1.2 Object..... 2
  - 1.3 Method..... 2
  - 1.4 Disposition..... 3
  - 1.5 Delimitations ..... 3
- Chapter 2 Theory..... 5
  - 2.1 Pile installing basics ..... 5
    - 2.1.1 Pile types..... 5
    - 2.1.2 Pile installation techniques..... 6
    - 2.1.3 Pile materials ..... 7
  - 2.2 Soil mechanics and parameters..... 8
    - 2.2.1 Soil overview ..... 8
    - 2.2.2 Soil mechanics ..... 9
    - 2.2.3 Dilatation and contraction ..... 11
    - 2.2.4 Porosity..... 12
  - 2.3 Pile-soil interaction ..... 13
    - 2.3.1 Pile driven in granular soil..... 13
    - 2.3.2 Pile driven in Clay ..... 14
  - 2.4 Summary of the soil models..... 14
    - 2.4.1 Mohr-Coulomb ..... 14
    - 2.4.2 Drucker-Prager ..... 16
  - 2.5 Peak Particle Velocity ..... 18
  - 2.6 Wave propagation ..... 18
    - 2.6.1 Pressure wave ..... 19

2.6.2	Shear wave.....	20
2.6.3	Rayleigh wave .....	21
2.7	Finite Element Method.....	21
2.7.1	Plane stress and plane strain.....	22
2.8	Dynamics .....	23
2.8.1	Newton’s second law.....	23
2.8.2	Damping.....	24
Chapter 3	Skövde field test .....	27
Chapter 4	Model set up.....	29
4.1	Introduction .....	29
4.2	Model.....	30
4.2.1	Geometry.....	30
4.2.2	Physics .....	31
4.2.3	Study set up.....	37
Chapter 5	Results .....	39
5.1	Steady State.....	39
5.2	Wave propagation .....	40
5.2.1	Pile depth 3 meters .....	41
5.2.2	Pile depth 11.5 meters.....	43
5.2.3	Pile depth 17 meters .....	45
5.3	Particle velocities .....	47
Chapter 6	Discussion and Conclusion.....	57
6.1	Discussion.....	57
6.1.1	Young’s modulus and vibrations.....	57
6.1.2	Material models.....	58
6.1.3	Comparison with Field test.....	58
6.1.4	Error sources .....	58
6.2	Conclusion .....	59
6.3	Further studies.....	60
	Bibliography.....	61

AppendixA.....	65
Coulomb criterion .....	65
Mohr's circle.....	65
Mohr-Coulomb failure criterion.....	67
AppendixB .....	69
Application of the finite element method .....	69



# Chapter 1

# Introduction

## 1.1 Background

Pile installation is a technique to reinforce the soil with poles in order to reduce settlements for structures, such as buildings or roads. There are many different types of pile driving techniques used for different types of conditions. The most common types of piles are made of wood, steel or concrete. These can be installed into the ground in a great variety of methods. The most common are:

- Drill and inject concrete as pillars, CFA
- Jacking
- Vibratory hammers
- Dropping weight

Performing an installation of a pile (a “pile drive”) affects the surrounding area from where the pile is installed. It is often associated with a great amount of noise and vibrations. When installing a pile, the effects on the surrounding area may be hard to predict. Vibrations from the installation will occur and these can cause deformation to the soil and damage nearby constructions. This is why it is of great importance to predict the impact that follows from the pile installation process.

This report focuses on the effects of vibrations from a concrete pile installation with a dropping weight. There are numerous methods for calculating and anticipating the deformations and vibrations in the surrounding soil. However, none of these are accepted to be a general solution. Many institutes, companies or authorities have their own way to implement their methods for computing the deformations and vibrations. Some make use of empirical data in a rule-of-thumb method while others are computing using advanced numerical methods.

Trying to model an accurate description of the soil, its layers and its characteristics is hard to do due to the fact that we often do not know exactly what’s underneath the surface (Hintze, et al. 1997). Predictions of deformations can always be made, but the exact values are sometimes hard to predict. According to the Swedish pile-commission, an order of priority has to be made when trying to analyse the given parameters associated with pile driving. The most important parameters in soil dynamics are (Hintze, et al. 1997):

- Wave propagation velocity,  $c$
- Poissons ratio,  $\nu$

- Material damping, D

With the results from an investigation of vibrations, one could predict deformations. This is especially helpful when doing an estimation of a safe distance to perform a pile installation or prevention measurements with respect to existing structures, in and on the soil.

## 1.2 Object

The object is to investigate the possibility of using a finite element software to predict vibrations in the surrounding soil while installing a pile. The course of action is to study the dynamic effects of a dropping weight pile installation at different pile depths, using the finite element method. The effect investigated is the vibration in the surrounding soil expressed in particle velocity. The results from the modelling will be compared with results from an actual field test. The questions at issue to be answered are:

- Can the vibrations due to pile installation be simulated realistically in a FE-model?
- What differences in results will different soil material models give?

## 1.3 Method

Models with an ideal stratigraphy are built and simulated in a finite element program. The models are based on a field test in Skövde made by Gunnar Nilsson in 1989 and with his results used in a paper by Massarsch and Fellenius in 2008. The actual material properties of the soil are modelled as well as pile installation conditions of that of the hammer. The model simulates a single impulse load at three different pile depths. The particle velocities are extracted at the surface at three different horizontal distances from the pile. The results are compared with the actual results of the field test made by Nilsson in 1989. When the models are compared, the particle velocities at different distances and depths in the soil are studied.

Parameters to investigate are:

- Vibrations at surface with horizontal distance of 10, 20 and 40 meters from the pile at different pile depths
- Differences in results with material models such as Mohr-Coulomb, Drucker-Prager
- Alteration in Young's modulus

## 1.4 Disposition

The report is divided into different chapters treating the following:

**Chapter 2:** This chapter contains the theoretic background necessary to understand what is executed in the following chapters. The topics at hand are: Pile installation basics with pile materials and pile types, a short overview of soil mechanics, summary of different soil models, wave propagation basics.

**Chapter 3:** An abridgement of the field test that is used as a model for this master's dissertation is presented.

**Chapter 4:** The set up for the finite element simulation is presented

**Chapter 5:** Results from the simulations are summarised and explained.

**Chapter 6:** Conclusions from the simulations are stated in this chapter as well as a discussion around the possible error sources.

## 1.5 Delimitations

The finite element computing will be done solely in the commercial FE-program COMSOL Multiphysics, a program with capacity of simulating various physical phenomena. All models will be made in 2D. The pile investigated is a pre-fabricated concrete pile and the method is a dropping weight pile installation. The analysis is based on the conditions of the field test made by Nilsson in 1989. The analysis is constrained to three different pile depths. The pile is only exposed to a single hammer blow, hence no respect of interfering waves due to multiple blows will be taken in consideration. The thesis investigates vibrations, not fracture mechanics.



## Chapter 2

# Theory

### 2.1 Pile installing basics

The main purpose of piles is to carry a structure when the ground bearing capacity itself is insufficient, and to transfer the loads to a better soil layer or bedrock surface. The main usage of piles in Scandinavia is concentrated to areas where there are thick layers of clay, mud etc. Piles are characterised and grouped based upon various criteria, for example their mechanism of load transfer, installation method and what materials the pile is made of. Since homogenous soil layers are rare in nature, it is difficult to categorise a single pile as a specific pile type. The pile can at different depths engage in stiff soils, granular soils and stiff/firm soils. This means piles of a certain type may carry loads differently at different spots in the same piling area. Nevertheless, categories are made of the different pile types to explain its main purpose and function.

#### 2.1.1 Pile types

##### **Cohesion piles**

For piles in cohesion soils, the load capacity is largely dependent on the cohesion between pile and soil. The tip bearing capacity is commonly only a fraction of the total capacity. This type of pile is usually used in cohesion soils such as clay. When installing a pile in such soils, the soil becomes moulded and therefore loses its strength. This means the bearing capacity of the pile does not reach its full potential until months later when the soil regains its strength. Cohesion soils do not compact as well as friction soils and mass displacement will occur. This results in horizontal soil displacement close to the pile. With increased distance to the pile, the soil will eventually heave. (Terzaghi, Peck, & Mesri, 1996), (Massarch & Wersäll, 2014).

##### **Friction piles**

Friction piles are used in granular soils with a great distance to firmer soils/bed rock. The bearing capacity is dependent on the surface friction of the pile as well as the end bearing capacity (Pålkommissionen, 2007). Piles installed in coarse-grained granular soils are called compaction piles due to their capacity to compress the soil and reduce the porosity of the soil when installed in groups. The load is transferred to the adjacent soil through side resistance, called skin friction. Piles installed in fine-coarse soils with low permeability are called floating piles. Unlike the

compaction piles they do not compact the soil in the same extent but transfer the load through side resistance (Terzaghi, Peck, & Mesri, 1996).

## End bearing piles

End bearing piles are common when the distance to soil layers/bed rock with good bearing capacity is reasonable (Pälkkommissionen, 2007). These piles transfer their load to through the pile to a firm layer such as rock.

### 2.1.2 Pile installation techniques

Piles that are installed into the ground using force of some kind to penetrate the soil are also called displacement piles. This is due to the fact that while installing the pile, the surrounding soil is displaced outwards, and sometimes downwards from the pile. Piles that are either bored or dug into the ground, fall under the category non-displacement piles. There are different types of machinery that are used for pile installation. A typical pile driver can be seen in Figure 1. A short introduction for the most common types are mentioned in the following sections (Terzaghi, 1986)

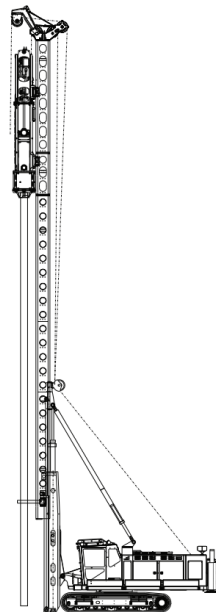


Figure 1 A typical pile driving rig

## Driven piles

The oldest, and most common type is the dropping weight hammer. As the name implies, a hammer is dropped upon the pile that is held in place by a rig and this forces the pile down in the soil. This is repetitively done until the pile ultimately is in its satisfactory position. Newer versions of the impact hammer is powered by hydraulics, steam or a diesel engine that gives the pile enough momentum to penetrate the soil. The newest pile driving hammer is the vibratory hammer, but since this hammer does not hit the pile “hard enough” it is not classified as an impact hammer (Adejumo, 2013). To make the soil less stiff before installing the pile, water can be pressed into the ground. This technique is called jetting. Jetting is only applicable if the soil

has large amounts of sand, since other fractions will make this inefficient (Ascalew & Smith, 2007). When installing a concrete pile, a cushion is often used on top of the pile to prevent damage on both the hammer and the pile while dropping the weight. Pile cushions can be made of several materials like wood, metal or plastic. A simplified sketch of a dropping weight hammer and pile cushion are presented in Figure 2.

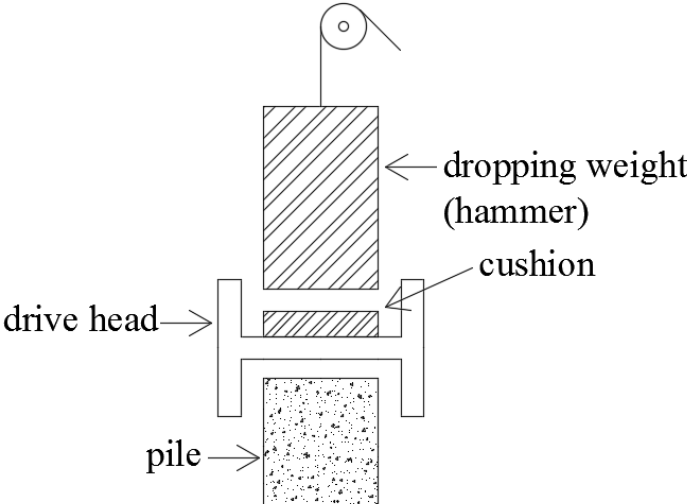


Figure 2 Simplified sketch of a dropping weight hammer

### Bored piles

Since a hole is dug before installation of the pile, and the pile installation will not affect the surrounding soil significantly, these piles are known as non-displacement piles. Bored piles will not be presented in this report.

### 2.1.3 Pile materials

#### Timber Piles

The oldest piles are made of timber. If the piles are placed under the water table i.e. always are exposed to water, the piles will last for a long time. Wooden piles are resistant to acids which make them suitable for use in contaminated soils. Some disadvantages of timber piles are that the piles cannot carry as much load as concrete or steel and that they are vulnerable for variations of the groundwater level (Reynolds, 2016).

#### Steel piles

Steel piles are often used as end bearing piles to great depths. Either the steel piles are made of solid steel or have a hollow core that is later filled with concrete. Steel piles are vulnerable to corrosion.

## Concrete piles

Concrete piles can be either precast or cast in place. The precast pile is often cast in lengths of about 10 meters since the length of the pile is limited by transportation issues. Figure 3 displays precast concrete piles. The piles are often made with prestressed reinforcement to prevent damage to the piles while installed. The concrete piles occur in different shapes with cross sections such as triangles, squares, octagonals or circles. They can easily be installed in long lengths using joints between the pile sections. The pre-cast pile can be damaged while installing if precautions or inaccurate methods are not taken care of.

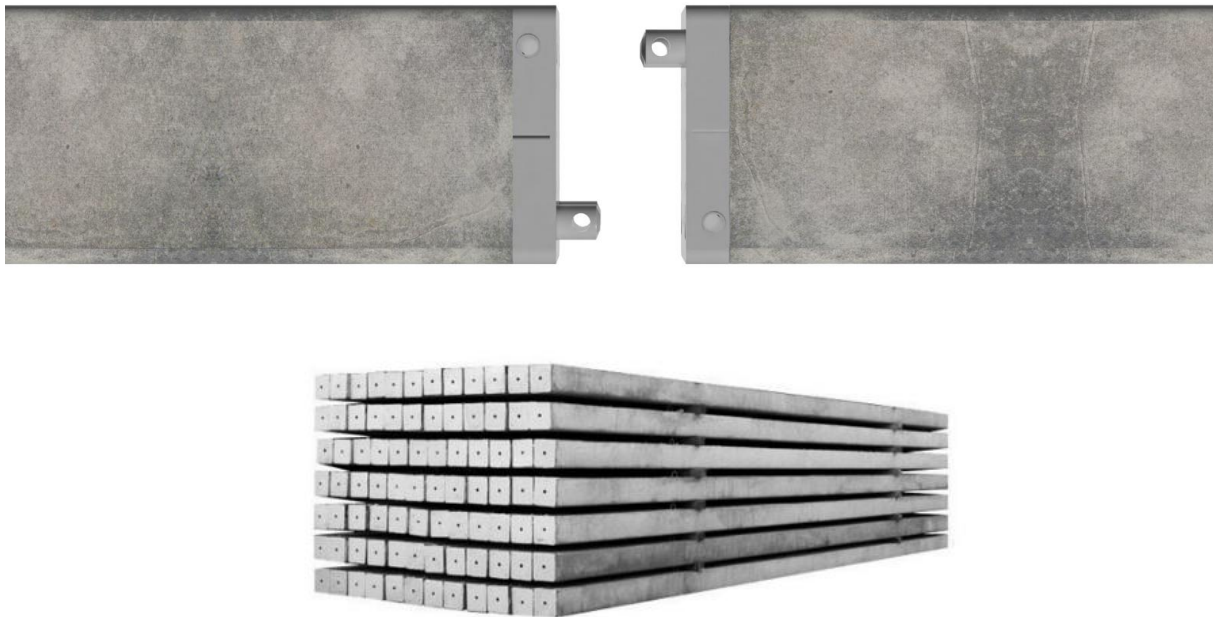


Figure 3 Top: Joint. Bottom: Precast concrete piles (EmecaSpe-USA, 2016)

## 2.2 Soil mechanics and parameters

### 2.2.1 Soil overview

Till is a glacial soil made of unsorted sediments which emanates from the ice ages and covers almost 75% of the Swedish land area (The Geological Survey of Sweden, [SGU], 2016). In Sweden, the latest glacial movements generated an erosion of the existing soils and rocks as well as a flow of existing relatively loose soil layers. The turbulent transportation of matter has given the till its unsorted characteristics. The till comprises the whole spectrum of grain fractions – from small particles of clay and silt through sand and gravel to big particles such as boulders and rocks. Depending on its origin and dominant fraction content(s), different till soils are at hand. Clay, sand, gravel or a mixture of some fractions can for example dominate a till (SGU, 2016).

A coarse size distribution of different types of solid particles according to Implementeringskommissionen för Europastandarder inom Geoteknik (2010):

Table 1 Size distribution for different fractions

Fraction	Grain size (mm)
Clay	< 0.002
Silt	0.002 – 0.063
Sand	0.063 – 2
Gravel	2 – 63
Cobble	63 – 200
Boulder	≥ 200

## 2.2.2 Soil mechanics

### Young's modulus

Young's modulus, or E-modulus, is the elastic modulus of a linear elastic material which describes the relationship between stress and strain. Young's modulus is expressed in Pa and can be described as:

$$E = \frac{\sigma}{\varepsilon} \quad (1)$$

with  $\sigma$  being the stress and  $\varepsilon$  the strain. This concludes that a great value of Young's modulus for a material means less strain compared to a material with a small value of Young's modulus exposed to the same stress.

### Poisson's ratio

Poisson's ratio,  $\nu$ , is a coefficient expressed in fraction or percent which describes the Poisson effect. This effect occurs when a material is exposed to compression or tension. If the material is compressed in one direction, the material will expand in the transverse directions. If the material is stretched in one direction, the material will contract in the transverse directions. Poisson's ratio describes this relationship of strain in the different directions as:

$$\nu = -\frac{d\varepsilon_{trans}}{d\varepsilon_{axial}} = -\frac{d\varepsilon_y}{d\varepsilon_x} = -\frac{d\varepsilon_z}{d\varepsilon_x} \quad (2)$$

with  $\varepsilon_{trans}$  being the transverse strain. For an isotropic linear elastic material, Poisson's ratio can range between  $-1.0$  and  $0.5$ . These limitations is due to requirements of Young's modulus, shear modulus and bulk modulus to have a positive value.

## Bulk modulus

The bulk modulus,  $K$ , describes a material resistance of uniform compression, i.e. the same magnitude of stress applied in all directions. The bulk modulus is expressed in Pa and can be described as:

$$K = -V \frac{dp}{dV} \quad (3)$$

with  $V$  being the volume,  $p$  being the pressure and  $\frac{dp}{dV}$  being the derivative of pressure with respect to volume. One can also express the bulk modulus in terms of pressure and density as:

$$K = \rho \frac{dp}{d\rho} \quad (4)$$

For an isotropic linear elastic material, the bulk modulus can also be expressed in terms of Young's modulus and Poisson's ratio as:

$$K = \frac{E}{3(1 - 2\nu)} \quad (5)$$

## Shear modulus

The shear modulus,  $G$ , describes the relationship between shear stress and shear strain expressed in Pa. The shear modulus can be described as:

$$G = \frac{F/A}{\Delta x/l} = \frac{F \cdot l}{A \cdot \Delta x} \quad (6)$$

with  $F$  being the shear force acting on the surface  $A$ .  $\Delta x$  is the transverse displacement and  $l$  is the initial length.

For a linear elastic isotropic material, the shear modulus can also be expressed in terms of Young's modulus and Poisson's ratio as:

$$G = \frac{E}{2(1 + \nu)} \quad (7)$$

## Total vertical stress in soil

A soil is structured by various particles compounded together. The particles all have different shapes and sizes but regardless of that there will be voids between these particles. The voids can be filled with gas, water or both. The vertical stress in a soil at a given depth depends on the overlying soil mass. The groundwater level also contributes to the vertical stress. The forces transmit through the particle skeleton as well as the water.

The total vertical stress can be described as:

$$\sigma = \sigma' + u \quad (8)$$

where  $\sigma'$  is the effective stress and  $u$  is the pore water pressure. The effective stress describes the stress carried out by the particles in the soil, while the pore water pressure describes the stress carried out in the water. The vertical stress with respect of depth,  $z$ , can be said to be depending on the bulk unit weight  $\gamma$  of its layers as:

$$\sigma = \int_0^z \gamma dz \quad (9)$$

### Horizontal stress

The horizontal stresses that occur in a soil are dependent upon the vertical stresses. A usual approach for calculating the horizontal stresses is to assume:

$$\sigma'_h = K_0 \sigma'_v \quad (10)$$

where  $K_0$  is referred to as the coefficient of earth pressure at rest (Terzaghi, Peck, & Mesri, 1996). From experimental data,  $K_0$  can be calculated as the ratio between the horizontal and the vertical stress. i.e.

$$K_0 = \frac{\sigma'_h}{\sigma'_v} \quad (11)$$

In the finite element program COMSOL Multiphysics the coefficient is instead calculated by the use of Poisson's ratio (Spetz, 2012), i.e.

$$K_0 = \frac{\nu}{1 - \nu} \quad (12)$$

By rearranging eq. 11 and inserting in eq. 12 and expression for computing the lateral stress at a specific depth in COMSOL Multiphysics can be obtained

$$\sigma'_h = \frac{\nu}{1 - \nu} \sigma'_v \quad (13)$$

### 2.2.3 Dilatation and contraction

When a soil is exposed to enough shear stresses, the volume tends to change. When the soil volume increases, this is due to a phenomenon called dilatancy. When the soil volume decreases this is called contraction. Loose granular soils are often compacted to smaller volumes, while dense granular soils increase their volume. As can be seen in Figure 4 there are two particle structures. The figure to the left represents a loose granular soil, with the particles arranged on top of each other. This creates lots of voids in the particle structure. The figure to the right represents a dense granular soil, with minimal void volume.

Suppose that the soil to left is exposed to shear stress. This causes the particle structure to change and become the right structure. The height difference, or displacement, of  $dH$  is denoted in Figure 4. Suppose the same thing again but with the voids filled with water. A displacement of

the particles will cause an increase in the pore water pressure. Since the shear resistance in a soil is dependent of the pore water pressure this can cause slope failures or soil liquefaction (Verruijt, 2012).

Suppose that the already dense granular soil in the figure (right) is exposed to shear stress. This causes the particles to rearrange as in the figure to the left. This means the soil volume increases, i.e. the soil will dilate.

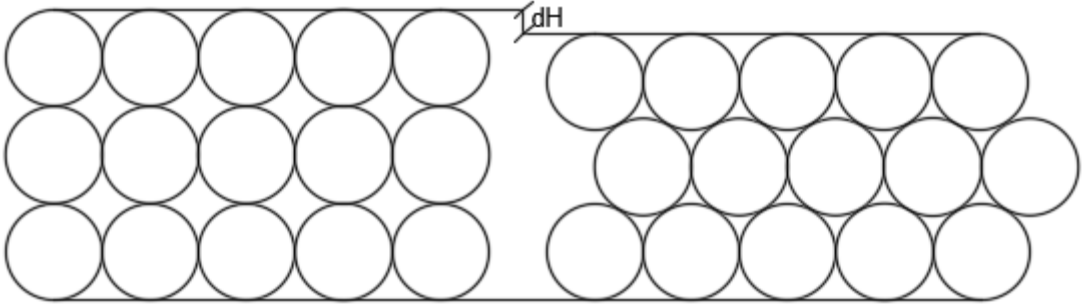


Figure 4 To the left: Loose Granular Soil. To the right: Dense Granular Soil

Since soils have a lot of voids it is necessary to take this into consideration while computing volume changes. In the Finite Element program COMSOL this is taken care of by introducing an angle of dilatation. As can be seen in Figure 5,  $\psi$  describes the minimum angle that the upper particle needs to translate in to achieve dilatation.

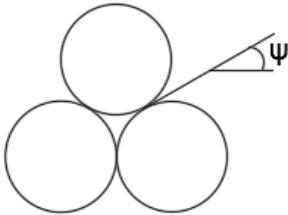


Figure 5 Presentation of the angle of dilatation,  $\psi$

The angle of dilatation for different soils depend on what shape the particles have. For instance, a clay with flake like particles, the angle is close to zero. On the other hand, for a soil with rounder particles the dilatation angle increases. For very loose granular soils the dilatation angle can be below zero (COMSOL, 2012) (Bartlett, 2012) (Sture, 2004).

For some granular soils, the angle of dilatation can be estimated as  $\psi = \phi - 30^\circ$ , where  $\phi$  is the angle of internal friction (Bartlett, 2012).

### 2.2.4 Porosity

A regular soil is a composition of air, water and solid particles. The voids that occur in the solid particle skeleton contains either water or air, or both, in different ratios. The equation for the porosity is

$$e = \frac{V_p}{V_t} \tag{14}$$

where  $V_p$  expresses the void volume and  $V_t$  the total volume. Some typical values for the porosity for a very mixed till can be down to 20 %, while for a loose sand the ratio can be 50 % (Terzaghi, Peck, & Mesri, 1996).

## 2.3 Pile-soil interaction

### 2.3.1 Pile driven in granular soil

According to Terzaghi, Peck & Mesri (1996) the skin friction,  $f_{s,gran}$ , along a pile driven in granular soil varies as

$$f_{s,gran} = K_0 \sigma'_v \tan \delta \tag{15}$$

where  $K_0$  is the coefficient for earth pressure at rest from eq. 12,  $\sigma'_v$  is the vertical stress and  $\delta$  is the friction angle between the soil and the pile. The force along the entire pile can thereby be described as

$$Q_{s,gran} = A_s \int_0^L K_0 \sigma'_v \tan \delta dz \tag{16}$$

where  $A_s$  is the circumference of the pile. Terzaghi, Peck & Mesri (1996) also suggested some values for the friction angle between the pile and the soil, as in Table 2. Figure 6 displays the friction along the pile shaft.

Table 2 Friction angles between different soils and concrete piles

Soil type	$\delta$ [degree]
Gravel	20-35
Sand/Gravel	20-35
Sand	20-40
Sand/silt	10-34

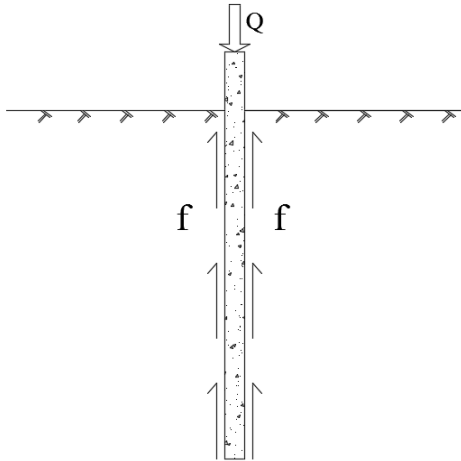


Figure 6 The friction along the pile is marked with "f" in the figure

### 2.3.2 Pile driven in Clay

If a pile is driven in a clay the equations will be quite different since the clay will be remoulded during the drive. An equation presented by Burland et. al. (1973) suggests that the friction along a pile driven in clay could be expressed without any cohesion between the pile and soil since the clay is remoulded. The equation takes the expression

$$f_{s,\text{clay}} = K_{0,\text{clay}} \sigma'_v \tan \phi' \quad (17)$$

where  $K_{0,\text{clay}}$  is the coefficient of earth pressure at rest for clay, which is  $K_{0,\text{clay}} = 1 - \sin \phi'$  and  $\phi'$  is the effective angle of internal friction. In a field test a pile was driven in a soft to medium clay, the effective angle of internal friction was concluded to be approximately 40 degrees. The total resistance force along the pile shaft for remoulded clay can thereby be expressed as (Cornfield, Haswell, & Burland, 1973)

$$Q_{s,\text{clay}} = A_s \int_0^L K_{0,\text{clay}} \sigma'_v \tan \phi' dz \quad (18)$$

## 2.4 Summary of the soil models

### 2.4.1 Mohr-Coulomb

A short summary of the Mohr-Coulomb criterion is presented in this chapter. For further reading, see Appendix A.

#### Drained Analysis

The oldest and most widely used soil model is the Mohr-Coulomb criterion (MC). As can be seen in eq. 19 the failure shear strength is a function of the cohesion, internal friction and the effective stress.

$$\tau_f = c + \sigma' \tan \phi \quad (19)$$

The conclusion is consequently that if the shear stress reaches the right hand side of the equation the soil will fail. The Coulomb failure line is often used in intercommunion with a Mohr's circle. As can be seen in Figure 7 a Mohr's circle is drawn with two intersects on the horizontal axis. The intersection to the right denoted as  $\sigma_1$ , is the first principal stress. The intersection to the left, denoted as  $\sigma_3$ , is the third principal stress. With greater differences in vertical-horizontal stress, the circle grows larger. Ultimately the circle tangents the  $\tau_f$ -line and the soil will fail. (Bartlett, 2012).

In a soil with a great cohesion constant the, MC criterion allows the soil to cope with tensile stresses. This is however not the case in most soils. In numerical modelling the MC criterion can

be quite cumbersome to apply since it contains singularities when used in three dimensions (Voyiadjis & Song, 2006). The MC failure criterion for an arbitrary soil in 2 dimensions can be seen in Figure 7.

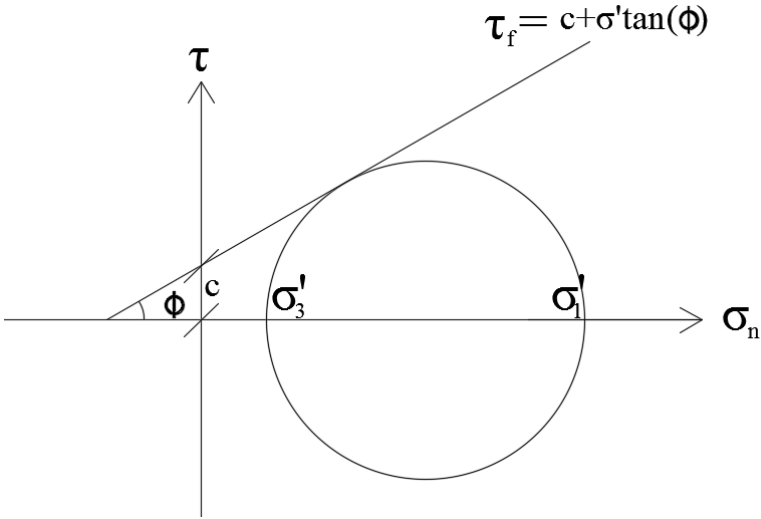


Figure 7 Mohr-Coulomb failure criterion in 2 dimensions

The singularities that the MC criterion holds become clearer in a three dimensional environment, as is shown in Figure 8.

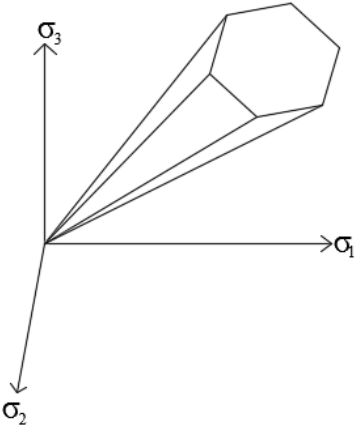


Figure 8 Mohr-Coulomb 3D failure surface

**Undrained analysis**

If a saturated soil is exposed to a rapid load, the pore water will not have enough time to dissipate. Instead, an undrained analysis must be performed. The saturation of the soil is considered to yield no friction between the particles and therefore the angle of friction becomes zero. Due to this the last term in Eq. 19 results in (Terzaghi, Peck, & Mesri, 1996):

$$\tau_{su} = c \tag{20}$$

In a two dimensional environment the failure line will appear as in Figure 9.

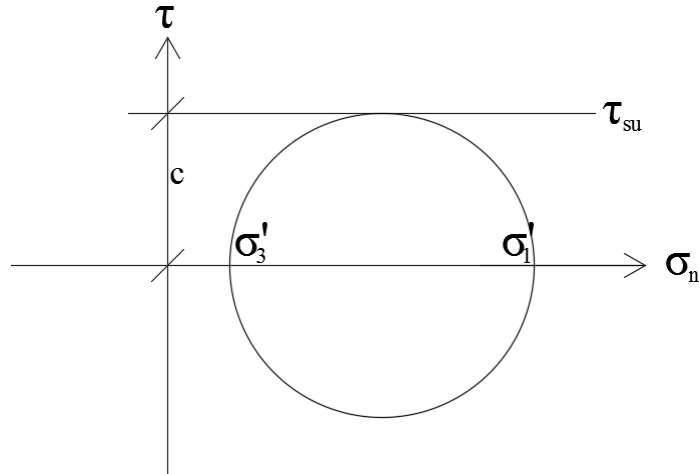


Figure 9 Undrained analysis

In three dimensions the failure surface will have a hexagonal shape as can be seen in Figure 10.

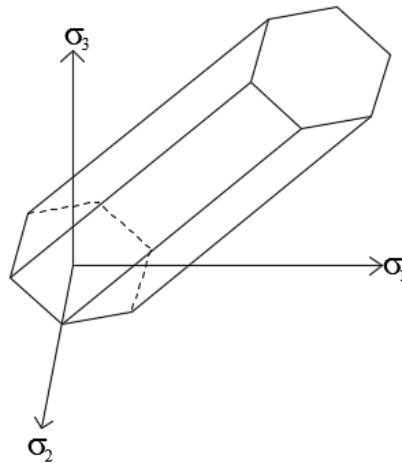


Figure 10 Undrained 3D

The undrained analysis has the same problem as the drained in regard to that the soil appears to be able to cope with tension stresses. Together with the singularity inconvenience, this is one of the biggest disadvantages with the Mohr-Coulomb model.

### 2.4.2 Drucker-Prager

1952 the German mathematician William Prager and the American engineer Daniel C. Drucker joined forces and published a generalised form of Mohr-Coulomb criterion. Since the Drucker-Prager (DP) originates from the Mohr-Coulomb criterion, it is dependent on the same variables, the cohesion, internal friction angle and the effective pressure (Alejano & Bobet, 2012). In numerical modelling the DP is often preferred since the failure surface encircles the MC criterion but does not contain any singularities that can interfere with the calculations (Voyiadjis & Song, 2006).

The DP criterion in three dimensions can be described as

$$\sqrt{J_2} = \lambda I'_1 + \kappa \quad (21)$$

where  $J_2$  the second invariant of the stress deviator tensor and  $I'_1$  is the first invariant of the stress tensor in which

$$\lambda = \frac{2 \sin \phi}{\sqrt{3}(3 - \sin \phi)} \quad (22)$$

$$\kappa = \frac{6c \cos \phi}{\sqrt{3}(3 - \sin \phi)} \quad (23)$$

$$J_2 = \frac{1}{6} [(\sigma'_1 - \sigma'_2)^2 + (\sigma'_1 - \sigma'_3)^2 + (\sigma'_3 - \sigma'_1)^2] \quad (24)$$

$$I'_1 = \sigma'_1 + \sigma'_2 + \sigma'_3 \quad (25)$$

where  $\sigma'_1$ ,  $\sigma'_2$  and  $\sigma'_3$  are the principal effective stresses,  $c$  is the cohesion,  $\phi$  is the internal angle of friction.

The DP failure surface can be adjusted to fit the MC criterion by modifying the equations that describe  $\lambda$  and  $\kappa$  for a more proper model. In Figure 11 the DP failure surface for an arbitrary soil can be seen.

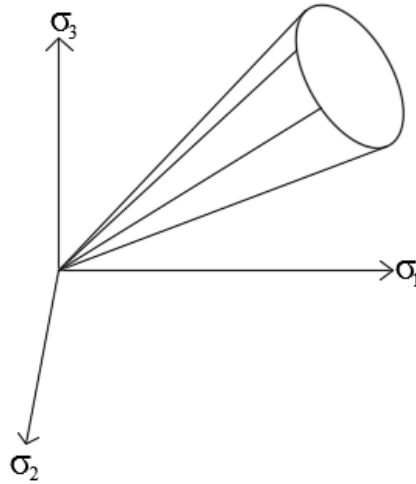


Figure 11 Drucker-Prager Failure surface

## 2.5 Peak Particle Velocity

To determine whether the vibrations from the pile drive can cause danger to nearby structures it is common to take a look at the particle velocities in different directions. The particle velocity,  $pv$ , is defined as

$$pv = \frac{\partial \delta}{\partial t} \quad (26)$$

where  $\delta$  is the particle displacement and  $t$  denotes the time. In a three dimensional environment the resultant particle velocity,  $Rpv$ , equals the square root of the summed squared velocities in respective direction, i.e.

$$Rpv = \sqrt{\left(\frac{\partial \delta_x}{\partial t}\right)^2 + \left(\frac{\partial \delta_y}{\partial t}\right)^2 + \left(\frac{\partial \delta_z}{\partial t}\right)^2} \quad (27)$$

The highest particle velocity that appears from the  $Rpv$  are referred to as the peak particle velocity,  $ppv$ . Carlsson & Massarch (1986) constructed the role model to Figure 12 which describes the  $ppv$  as a function of the frequency of how the much buildings are affected.

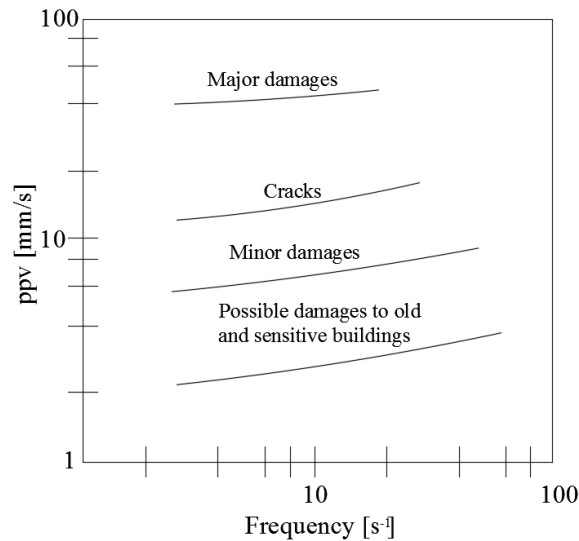


Figure 12 Peak particle velocity - Frequency plot

According to Massarsch & Fellenius (2008) the frequencies due to a pile driving process stay within the range of 8 to 15 Hz.

## 2.6 Wave propagation

Vibrations that are generated in the proximity of ground works due to explosions, pile driving and vehicles are commonly called ground vibrations. The vibration transfer process can be

separated in several different segments. These all contribute to the amplitude, the frequency and for how long the ground will vibrate (Hall & Wersäll, 2013).

The first segment named by Hall & Wersäll (2013) is the vibration source itself. Some vibration sources are mentioned below:

- Vibrations from rock blasting
- Construction vehicles
- Pile driving
- Traffic and railroad traffic
- Seismic events

All of these activities induce dynamical forces in the soil. The forces cause stresses in the ground that spread through the soil in different types of waves. In soil dynamics there are three different types of waves that are meant to be the most important. Two of which are body waves while the third is a surface wave. The three different waves all have dissimilar properties regarding speed, spread, frequency and travel distance. The body waves are called pressure waves (p-waves) and shear waves (s-waves). The surface wave is called Rayleigh-wave (R-wave). An introduction of the wave types will be presented shortly below.

### 2.6.1 Pressure wave

The pressure wave is the fastest of the body waves, and that's why it is also called primary wave. The pressure wave first compresses the body, then elongates it. The particle movement is the same direction as the wave propagates, this also implies that there are no rotation or shearing on the particles while the wave propagates (Deckner, 2013). Since soil has a much greater stiffness modulus for compression than for shear, the pressure wave travels faster than the other waves (Hall & Wersäll, 2013). According to Kramer (1996) and Möller et al. (2000) the wave propagation velocity,  $c_p$  [m/s], for the p-wave in different media can be calculated by

$$c_p = \sqrt{\frac{E(1 - \nu)}{\rho(1 - 2\nu)(1 + \nu)}} \quad (28)$$

where  $E$  is the elasticity modulus [Pa],  $\nu$  is Poisson's ratio [-],  $\rho$  is the density of the material [kg/m<sup>3</sup>]

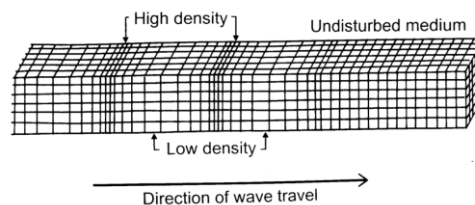


Figure 13 P-wave propagation (Landstreet, 2009)

Some typical pressure wave velocities are mentioned by Massarch & Fellenius (2008) and are summarised in Table 3.

Table 3 Pressure wave velocities in soils and water (Massarsch & Fellenius, 2008).

Soil type	$v_p$ [m/s]
Water	1450
Glacial Till	600- 1800
Dry Gravel	500- 1000
Saturated Gravel	1450
Saturated Sand	1450
Stiff Clay	1450

### 2.6.2 Shear wave

The s-wave is called secondary wave since its velocity is (almost) always the second fastest compared to the p-wave. The propagation of the s-wave has some resemblance with the movement of a snake, with its transversal movement of the particles (Möller et al. 2000). Due to the fact that shear waves causes shear deformation, s-waves can only travel through the particle skeleton, and not through the voids or viscous media. Figure 14 captures this movement. The wave propagation velocity  $c_s$  [m/s] is given by:

$$c_s = \sqrt{\frac{E}{\rho 2(1+\nu)}} \quad (29)$$

where,  $E$  is the elasticity modulus [Pa],  $\nu$  is the Poisson's ratio [-] and  $\rho$  is the density of the material [ $\text{kg}/\text{m}^3$ ]

As can be seen in the formulas for  $c_s$  and  $c_p$  the velocities are dependent on is the Poisson's ratio. For an average non saturated clay the Poisson's ratio is 0.4. This results in that the p-wave is close to 20 % faster than the s-wave. A lower value of the Poisson ratio yields a higher difference.

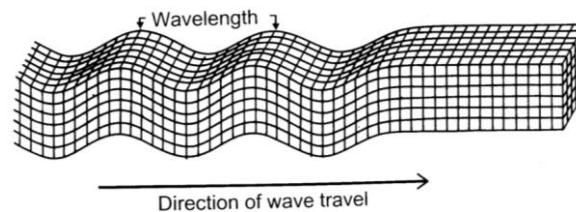


Figure 14 Shear wave propagation (Landstreet, 2009)

Table 4 Shear wave velocities in soils and water(Massarsch & Fellenius, 2008).

Soil type	$v_s$ [m/s]
Water	-
Glacial Till	300- 600
Dry Gravel	250- 400
Saturated Gravel	300- 400
Saturated Sand	150- 250
Stiff Clay	100- 200

### 2.6.3 Rayleigh wave

The Rayleigh-wave is the most common surface wave regarding soil dynamics. The Rayleigh-wave is a combination of both the pressure wave and the vertical component of the shear wave. A Rayleigh-wave can only exist if there is a free surface, through which the wave propagates. The particle movement in the wave is elliptical. Since the velocity of the Rayleigh-wave velocity is dependent on the p and s-wave the velocity equation can be quite cumbersome. An approximation can be (Lin, 2013)

$$c_R = \frac{0.87 + 1.12\nu}{1 + \nu} \cdot c_S \quad (30)$$

where  $\nu$  is Poisson's ratio and  $c_S$  is the shear wave velocity

The velocity is usually within the range of 87% to 96% of the shear wave. A typical Rayleigh-wave propagation can be seen in Figure 15. The ellipse that are shown in the figure denotes the particle movement.

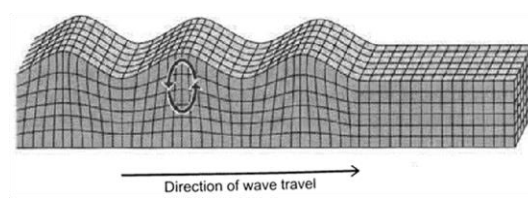


Figure 15 Rayleigh wave propagation (Landstreet, 2009)

## 2.7 Finite Element Method

This section concerns a general introduction to the finite element method. For further reading, see Appendix B, Application of the finite element method

A partial differential equation is an equation, which describes unknown functions and its derivatives. The partial differential equations can be used for describing a wide variety of physical events such as fluid and heat flow, electrostatics and mechanics. The definition for a partial differential equation of the function  $u(x_1, \dots, x_n)$  can be set as:

$$F\left(x_1, \dots, x_n, u, \frac{\partial u}{\partial x_1}, \dots, \frac{\partial u}{\partial x_n}, \frac{\partial^2 u}{\partial x_1 \partial x_1}, \dots, \frac{\partial^2 u}{\partial x_1 \partial x_n}, \dots\right) = 0 \quad (31)$$

A numerical analysis uses approximation for calculating and getting a solution as close to reality as possible.

The FE-method is based upon the concepts of dividing a global domain into smaller finite parts, called finite elements combining them into a so called finite element mesh. These elements are assigned their own local equations for approximating the global domain for the specific elements. The elements are put together and combined into the global domain for a global system of equations. With the use of initial boundary conditions and parameter values, the global system of equations can be calculated and a result of interest can be obtained. With the right use of the

finite element method, one can obtain a solution which is sufficiently close for describing reality. (Ottosen & Petersson, 1992)

When dividing the global domain into elements, every element has nodes along its boundary. Every node,  $j$ , is defined in a function  $\phi_j(\mathbf{x})$ . This function is continuous over the global domain but only different from zero over the area specified by the element. The solution for the equation is approximated as:

$$\mathbf{U} = \sum_{j=1}^N U_j \phi_j(\mathbf{x}) \quad (32)$$

where  $U_j$  is the weighting function.

The FE-formulation describes the relations of forces over its element boundaries with the displacements and stiffness of the object studied. The FE-formulation becomes:

$$\int_V \mathbf{B}^T \mathbf{D} \mathbf{B} dV \mathbf{a} = \int_{S_h} \mathbf{N}^T \mathbf{h} dS + \int_{S_g} \mathbf{N}^T \mathbf{t} dS + \int_V \mathbf{N}^T \mathbf{b} dV + \int_V \mathbf{B}^T \mathbf{D} \boldsymbol{\varepsilon}_0 dV \quad (33)$$

The FE-formulation written in a compact form is:

$$\mathbf{K} \mathbf{a} = \mathbf{f}_b + \mathbf{f}_1 + \mathbf{f}_0 \quad (34)$$

with

- $\mathbf{K}$  being the stiffness matrix consisting of the stiffness parameters
- $\mathbf{a}$  being the displacement vector consisting of the displacements for the elements
- $\mathbf{f}_1$  being the forces in the system

With the use of the mesh, calculations can be made on a vast variety of physical phenomena. For further reading of the Finite Element Method, see Appendix B- Application of the Finite Element Method

### 2.7.1 Plane stress and plane strain

In COMSOL Multiphysics one can choose whether the 2 dimensional study shall be performed in plane strain or in plane stress. In the plane stress study, the stress in the direction perpendicular to xy-plane is set to zero according to

$$\boldsymbol{\sigma} = \begin{bmatrix} \sigma_{xx} & \sigma_{xy} & 0 \\ \sigma_{yx} & \sigma_{yy} & 0 \\ 0 & 0 & 0 \end{bmatrix} \quad (35)$$

In the plane strain case the strain perpendicular to the xy-plane is set to zero according to

$$\boldsymbol{\varepsilon} = \begin{bmatrix} \varepsilon_{xx} & \varepsilon_{xy} & 0 \\ \varepsilon_{yx} & \varepsilon_{yy} & 0 \\ 0 & 0 & 0 \end{bmatrix} \quad (36)$$

Plane strain is used in the simulations in this report, due to the fact that the stresses in the soil matter also in the direction perpendicular to the xy-plane. The strains however can be neglected in this direction since they are very small in comparison to the x and y direction.

## 2.8 Dynamics

### 2.8.1 Newton's second law

Dynamics is the study of motions of particles and bodies under the influence of an applied force. The study often concerns developments of systems over time. Newton's second law describes the relationship of forces and acceleration:

$$\mathbf{F} = \frac{d\mathbf{p}}{dt} \quad (37)$$

where  $\mathbf{p} = m\mathbf{v}$  is the momentum,  $m$  is the inert mass and  $\mathbf{v}$  is the velocity. Since acceleration is the derivative of the velocity with respect of time, the equation can be written as:

$$\mathbf{F} = m \frac{d\mathbf{v}}{dt} = m\mathbf{a} \quad (38)$$

This means the force  $\mathbf{F}$  is the resultant force giving the mass  $m$  an acceleration  $\mathbf{a}$ .

An impulse is a force acting over a time interval. Since the force is a derivative of momentum, the impulse can be described as:  $s$

$$J = \int_{\Delta t} \mathbf{F} dt = \int_{\Delta t} \frac{d\mathbf{p}}{dt} dt = \Delta\mathbf{p} = m\Delta\mathbf{v} \quad (39)$$

### Impact speed

While installing a pile with a dropping hammer, a weight is dropped on the pile head. The force of which this hammer hits the pile is dependent on how far the hammer is dropped, and the mass of the hammer. The force distributed over the impact time will vary non-linear. The function for this will be derived in this section. A simplification is made under the assumption that the weight only will translate in the vertical direction. Since the distance of which the weight is dropped is relatively short, the air resistance is neglected as well as the possible friction between the dropping weight and the rig.

A falling object gains its speed by converting the potential energy to kinematic energy. An expression for the potential energy,  $W$ , can be seen in

$$W = mgh \quad (40)$$

where  $m$  is the mass of the object,  $g$  is the gravitational acceleration,  $h$  is the height.

Since change in potential energy is converted to kinetic energy gives

$$W = \Delta K \quad (41)$$

The kinetic energy is expressed as

$$K = \frac{1}{2}mv^2 \quad (42)$$

where  $v$  is the velocity, m/s

Expressing eq. 41 in terms of eq. 42 and eq. 40 concludes

$$mgh = \frac{1}{2}m(v_2^2 - v_1^2) \quad (43)$$

Assuming  $v_1 = 0$  and rearranging Eq. 43 yields

$$v_2 = \sqrt{2gh} \quad (44)$$

## 2.8.2 Damping

### Damped system

In a damped system, the force  $f_s$  can represent a spring, a viscous element or a frictional system. For the viscous system,  $f_s$  being a function of displacement and velocity after the Kelvin model (Austrell, 2016):

$$f_s = f_s(u, \dot{u}) \quad (45)$$

$$f_s = ku + c\dot{u} \quad (46)$$

where  $k$  is the stiffness,  $u$  is the displacement,  $\dot{u}$  is the velocity and  $c$  being the viscous damping coefficient [ $N \cdot s/m$ ], the equation for undamped motion can be written as:

$$p(t) = m\ddot{u} + c\dot{u} + ku \quad (47)$$

For viscously damped free vibrations, the equation 47 can be written as:

$$m\ddot{u} + c\dot{u} + ku = 0 \quad (48)$$

Rewriting the equation gives :

$$\ddot{u} + 2\zeta\omega_n\dot{u} + \omega_n^2u = 0 \quad (49)$$

since the natural frequency is  $\omega_n = \sqrt{\frac{k}{m}}$  and  $\zeta = \frac{c}{2m\omega_n}$  being the dimensionless damping ratio.

In a damped system the motion will slow down and eventually stop due to loss of energy in the system. The amplitude will start with an initial value and then gradually decrease. The main damping will be due to friction or viscous damping. There are 3 classes of damping:

- Underdamped
- Critically damped
- Overdamped

The **underdamped** system will oscillate and gradually decrease in amplitude due to its loss of energy each cycle. Figure 16 illustrates this. The underdamped system has a damping ratio of  $0 \leq \zeta < 1$ . Imagine a pendulum which starts at a given position. This pendulum will oscillate but due to damping, such as friction and air resistance, it will eventually stop. For every oscillation, the amplitude will decrease, i.e every swing will be a little bit shorter.

The **critically damped** system is a system which will be damped in such way that it never has the chance to oscillate. It starts out from its original position and then reach equilibrium without oscillating. The critically damped system has a damping ratio of  $\zeta = 1$ . If the recently mentioned pendulum would be in a space of a very viscous material, one could imagine the pendulum would have a hard time to swing. Instead, it would (relatively) slowly reach equilibrium without oscillating, see Figure 16. The swing would be slower than the first oscillation in the undamped system, but the critically damped system will reach equilibrium fastest of the three damping classes. This is because it does not oscillate, as in the undamped system.

The **overdamped** system is a system that resembles of the critically damped system, but it takes much longer time for it to reach equilibrium. Once again, see Figure 16. The overdamped system has a damping ratio of  $\zeta > 1$ . Imagine the pendulum being in a space much more viscous or frictionous than the critically damped system. It will not oscillate, the same as in the critically damped system, but it will take a longer time to get from its initial position to reach equilibrium.

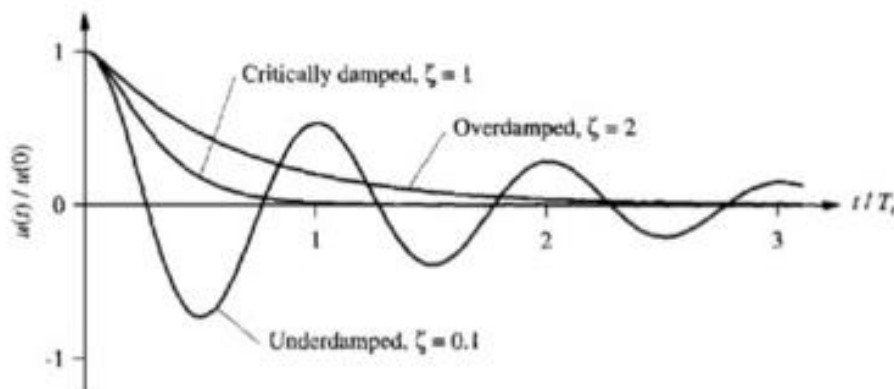


Figure 16 Illustration of displacements with respect of time in systems with different damping properties (Austrell, 2016)

For an underdamped system ( $0 \leq \zeta < 1$ ) the displacement will decrease exponentially with respect of time as:

$$u(t) = e^{-\zeta\omega_n t} \cdot [u(0) \cos \omega_D t + \frac{\dot{u}(0) + \zeta\omega_n u(0)}{\omega_D} \cdot \sin \omega_D t] \quad (50)$$

where  $\omega_D = \omega_n \sqrt{1 - \zeta^2}$

For an undamped system with  $\zeta = 0$ , this can be rewritten as

$$u(t) = [u(0) \cos \omega_n t + \frac{\dot{u}(0)}{\omega_n} \cdot \sin \omega_n t] \quad (51)$$

### Soil damping

As previously stated a material consumes energy while it deforms. The material damping is commonly expressed in a percentage number of the critical damping. For a soil with an elastic deformation the material damping can be set to somewhere between 3 and 6 percent (Massarsch & Fellenius, 2008) (Hintze, o.a., 1997).

### Hammer damping

When the hammer hits the pile, some energy will be lost. Some of this energy loss can be traced back to the damping in the hammer, the pile cushion and the pile. Rausche (2000) has mentioned that for a free fall hammer the energy loss will be circa 10 percent (Rausche, 2000). Hammer cushions from the American company Advanced Products & Systems, Inc. are displayed in Figure 17

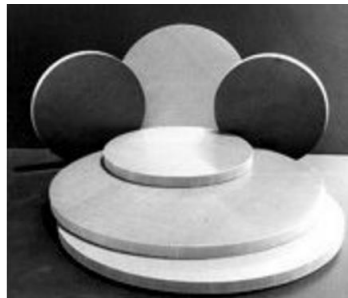


Figure 17 Hammer cushions from Advanced Products & Systems, Inc.

## Chapter 3

# Skövde field test

In 1989 Gunnar Nilsson made a series of measurements from a pile drive in proximity to the town Skövde in Västergötland county, Sweden. The results from this field test have been part of a paper from Massarsch & Fellenius, 2008.

The results from the field test are compared with results from the simulations. Nilsson arranged vibration sensors of 10, 20 and 40 meters distance respectively from the pile site. The geophones used measured particle vibration velocities vertically (V1, V2, V3), and vibration velocities horizontally (H4) at the surface of the soil, see (Massarsch & Fellenius, 2008). The pile depths focused in this report will be as follows:

- 3m
- 11,5m
- 17m

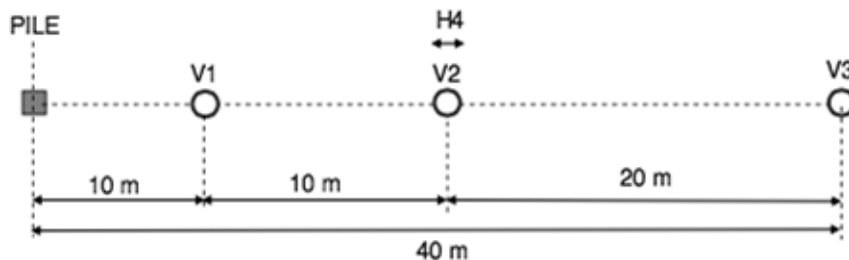


Figure 18 Arrangement of vibration sensors during driving of the test pile. V1, V2 and V3 indicate vertical geophones and H4 indicate horizontal geophones. (Massarsch & Fellenius, 2008)

### Geotechnical soil profile at the test site

Table 5 Soil profile at test site in Skövde, with the fill at the surface and the glacial till in the bottom

Soil	Layer thickness (m)	Stiffness/Strength (kPa)	Density (kg/m <sup>3</sup> )	Assumed shear wave speed (m/s)	Poisson's ratio
Fill (slag and sand)	3	-	1900	150-200	0.3
Clay	12	30	1600	100-150	0.5 (0.495)
Sand and Gravel	7	Loose to dense	1800	250-350	0.3
Glacial Till	3	Stiff	1900	400-600	0.3

The pile installed was a reinforced concrete pile of a square cross section, 270x270mm, a bulk density of 2400 kg/m<sup>3</sup> and impedance  $Z^P = 714\text{kNs/m}$ . Impedance is a measure of resistance to motion of a structure subjugated to a force. The pile was made by three segments of 13.3, 10 and 6 meter making a total of 29.3 meter. The weight and length of the hammer was 4000 kg and 3.65 meters respectively and fell from 0.40 meter per blow (except for the last blows at 25 meter, then used 0.50 meter per blow).

Recordings of the vibration frequency was made with the results of that the dominant frequency of the waves ranged from 8 through 15 Hz at all locations of vertical measurements. At the point with horizontal recording (H4) the spectra of particle velocity was wider than of the vertical, with dominant frequency at 45 Hz.

In the report (Massarsch & Fellenius, 2008), it is acknowledged that the vertical vibrations decrease markedly with the horizontal increase in distance from the pile, see Figure 19. Also noted should be that cylindrical waves dominate when the pile is installed in the upper soil layers while spherical waves from the pile toe dominate when the pile toe reaches through the stiff till. One can also note that when the pile toe reaches a depth of 17-25 meters the measured vibration at distance 10 and 20 meters (V1 and V2) are almost the same. The direct distance from the pile toe to the measuring point is hereby 26 and 32 meters respectively which gives only a small difference in wave propagation, explaining the small difference in measured results. The value of wave propagation velocity was calculated with the information of particle velocity and time of the hammer impact, which resulted in an average of 125 through 175 m/s in the upper layers (Massarsch & Fellenius, 2008).

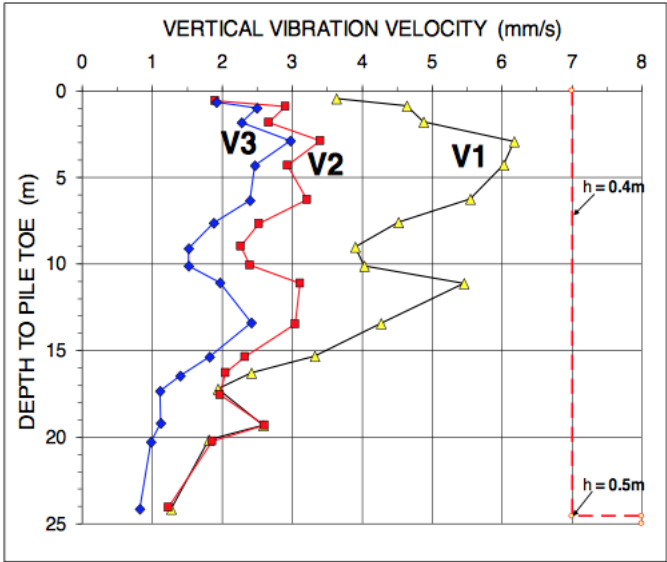


Figure 19 Maximum vertical vibration velocities at different depths and horizontal distances (Massarsch & Fellenius, 2008)

## Chapter 4

# Model set up

### 4.1 Introduction

The numerical analysis of the wave propagation and vibrations are made with the commercial FE-software COMSOL Multiphysics version 5.2 with the Geomechanics module. The geometry and material properties that were available from the field tests by Nilsson (1989) are used. The values that could not be provided from the test are estimated standard values. Numerous calculations with altering pile depth have been made and the results are compared with the results from Nilsson (1989).

Vibrations in the soil are studied when the pile is subjected to a single hammer blow. The vibrations have been studied at three locations on the surface for three different pile depths. The locations of the studied points at the surface are located at a horizontal distance of 10, 20 and 40 meters from the pile. A parametric study of extreme values of Young's modulus is performed due to lack of information of soil properties. After being compared with the actual field test results, studies of the peak particle velocity (PPV) are made at different points of interest.

The study of particle velocities with alternation of Young's modulus is made for three different soil models:

- Linear-elastic model
- Mohr-Coloumb failure criterion
- Drucker-Prager failure criterion

The solid mechanics physic in COMSOL Multiphysics is used.

# 4.2 Model

## 4.2.1 Geometry

A 2D geometry of the soil and pile is built up with the geometry tool in COMSOL Multiphysics. Since the surroundings of the test site are considered to be homogenous, a symmetry line is created in the middle of the pile. The soil layers in COMSOL Multiphysics are built up according to Table 5, see Figure 20. A soil width of 300 meters and a total soil depth of 97 meters is chosen to prevent the effects of boundary reflections.



Figure 20 Geometry in 2D with symmetry in consideration

Just underneath the pile is a domain of soil with the same width as the pile. This domain is created to easily be adjusted when creating studies at different depths of the pile, see Figure 21.

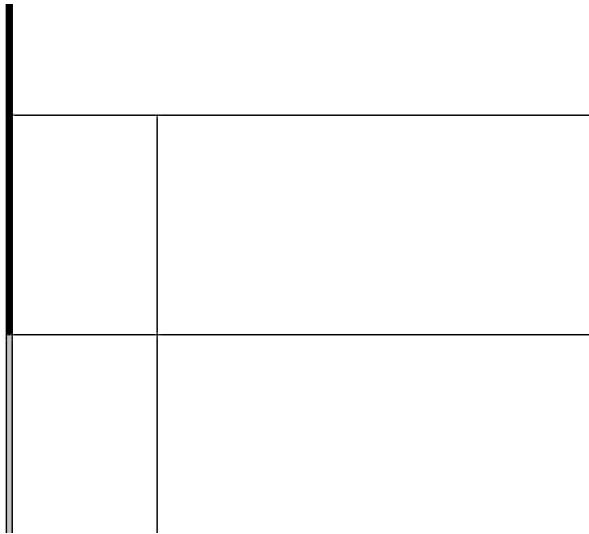


Figure 21 Zooming of the pile (black) and the adjustable soil domain (grey)

## 4.2.2 Physics

### Boundary conditions

In this 2D model, the thickness of the geometry used is 0.27 meters, the same thickness as the pile.

The model has a fixed boundary constraint in the bottom to prevent the boundary from moving in any direction. This is an approximation based on the assumption that the stiff soil underneath is (relatively) incapable of moving. The effect of having the approximation is that propagating waves will reflect on the boundary.

A roller constraint is put on the right side boundary to prevent the soil from moving in horizontal direction but enable it to move in the vertical direction. Due to the great wave propagation velocities the distance from the pile to the right side boundary is set to 150 meters. This is assumed to be at a sufficient distance for the waves not being able to interfere when reflecting at the boundary during the simulations.

A symmetry boundary is put on the left side, including both the soil and the pile. This boundary represents the real situation when the soil and pile have the same distribution on the left hand side.

The contact between the soil and the pile is hard to model for a FE-program. To make the contact possible, it is modelled with a thin elastic layer (TEL). This means a thin layer is placed between the pile and the soil with springs making it possible for the domains to move and still be in contact. The spring property values are chosen to represent adhesion and friction. The springs in vertical direction along the domain boundary represent the friction and adhesion between soil and pile, section 2.3. The springs in the horizontal direction are used to keep the domains in contact but not overlap.

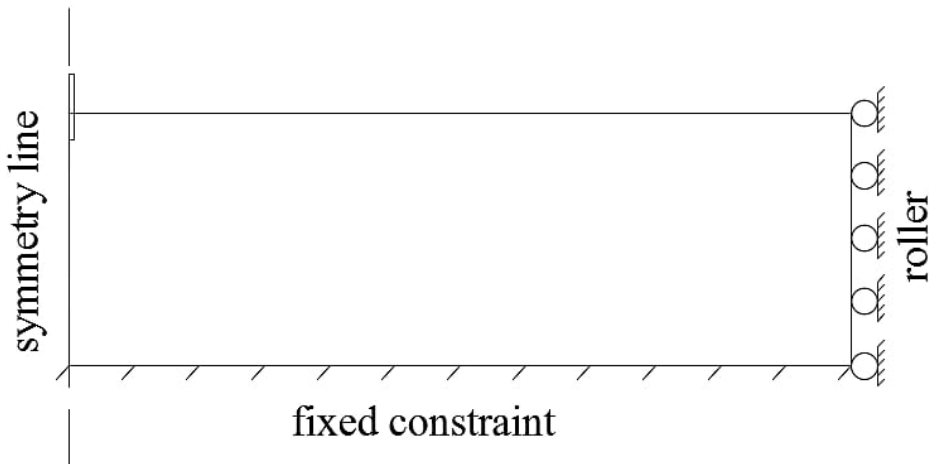


Figure 22 Illustration of boundary conditions

## Impact load

The impact load of the hammer is placed as a boundary load in the negative vertical direction on the top boundary of the pile. The boundary load derives from the weight of the hammer and the height of the fall. With a drop of  $h = 0.4$  meters, a mass of  $m = 4000$  kg and the effective ratio of  $\eta = 0.9$  due to the damping of the cushion, the impact momentum can be described as:

$$I_{\text{impact}} = \sqrt{2gh} \cdot m \cdot \eta \quad (52)$$

A rectangle function is used to represent the impulse. The hammer starts to act on the boundary at time 0,01s instantly during 0,1 second of time. Thereafter the hammer is unloaded instantly. This procedure represents the impulse of the hammer blow, see Figure 23. The time duration is an approximation after Rausche (2000)

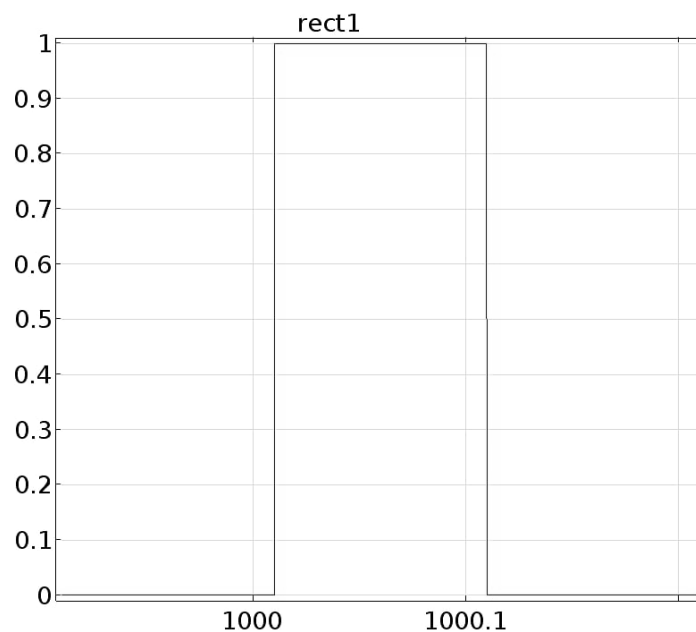


Figure 23 Rectangle function used for impulse load

With the use of the rectangle function, the expression of the load in eq.52, can be combined with the rectangle function so it acts during that time interval. The syntax in COMSOL Multiphysics when applying the boundary load  $F_{\text{tot}}$  in the vertical direction:

$$F_{\text{tot}}(y) = -\text{impact\_drop} \cdot 0,5 \cdot \text{rect1}(t[1/s]) \quad (53)$$

With  $\text{impact\_drop}$  being the load,  $\text{rect1}(t[1/s])$  being the rectangle function with respect of time and 0,5 being used due to symmetry in the model.

**Material models**

In Figure 24, the Drucker-Prager and Mohr-Coulomb yield surfaces are illustrated. For the Drucker-Prager model the circle that is denoted as “inner fitting” is the one used in the forthcoming simulations. The use of the inner circle reaches plastic deformation in an earlier stage and can thereby be seen as a more restrictive approach regarding plasticity.

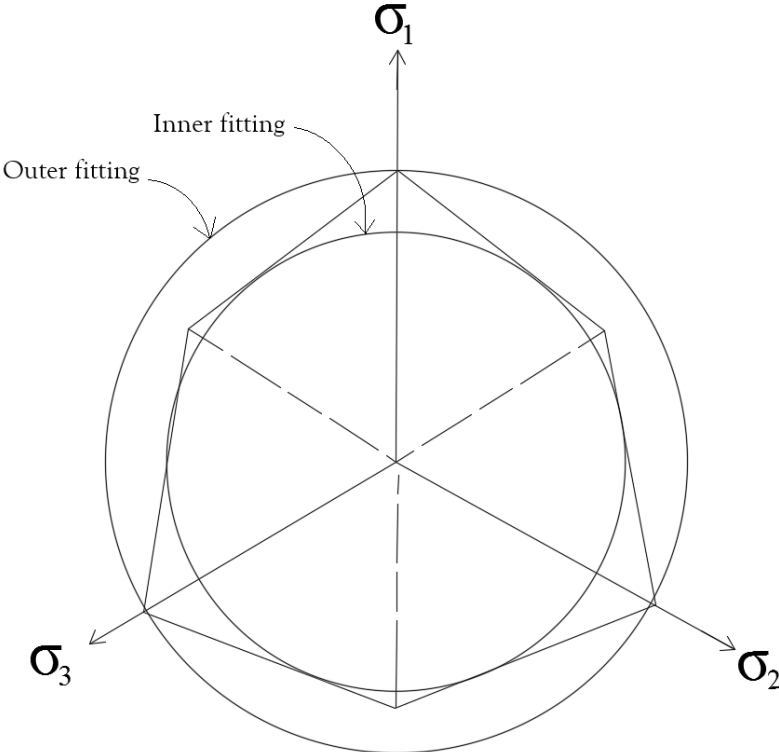


Figure 24 Drucker-Prager (circles) and Mohr-Coulomb (hexagonal) failure surfaces

## Material properties

A parameter study is made where Young's modulus are altered. Since the bulk modulus  $K$  and shear modulus  $G$  is dependent of Young's modulus, they are altered as well. The alternation is made to find a behaviour in the model representing the real behaviour of the velocities in the field test. This is due to the lack of soil parameter information in the field test performed by Nilsson in 1989. The input parameters are extracted from standard material properties, in this case from USACE (Info, 2012).

The material properties for the parameter study performed can be seen in Table 6. Since only the Young's modulus will be altered, only the parameters that are affected are displayed in Table 8. The soil is assumed to be isotropic. The angle of the friction in clay is considered to be zero, to simulate an undrained analysis.

The material partitioning for the model is illustrated in Figure 25.

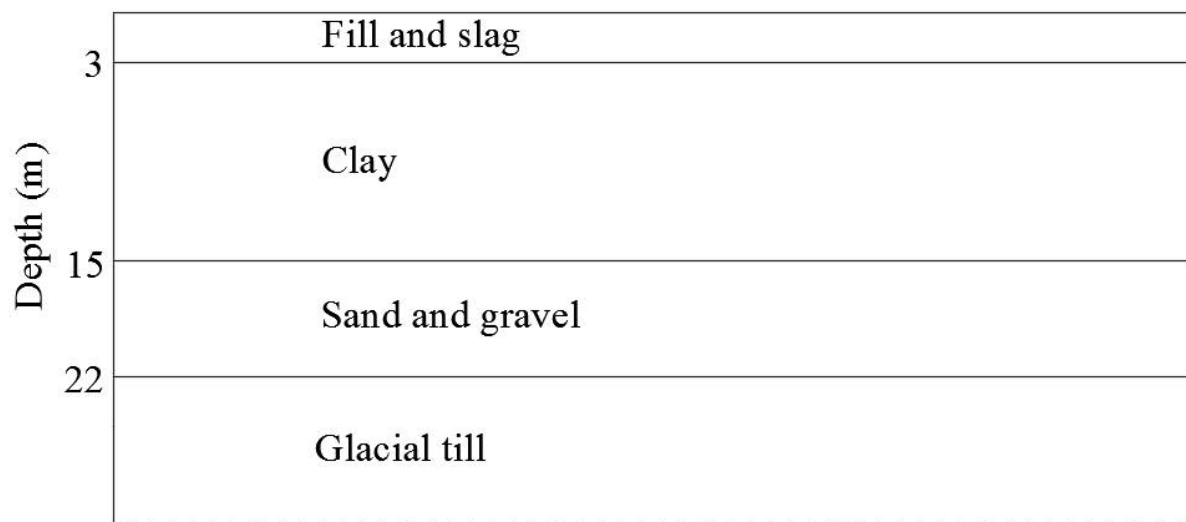


Figure 25 Material partitioning

Table 6 Material parameters for the minimum value of Young's modules

	$\nu$	$E_{\min}$ (N/m <sup>2</sup> )	$K_{\min}$	$G_{\min}$
Glacial Till	0.3	$1.44 \cdot 10^8$	$1.2 \cdot 10^8$	$5.54 \cdot 10^7$
Sand and Gravel	0.3	$4.8 \cdot 10^7$	$4.0 \cdot 10^7$	$1.85 \cdot 10^7$
Clay	0.495	$1.5 \cdot 10^7$	$5.0 \cdot 10^8$	$5.02 \cdot 10^6$
Fill and Slag	0.3	$4.8 \cdot 10^7$	$4.0 \cdot 10^7$	$1.85 \cdot 10^7$

Table 7 Material parameters for the maximum value of Young's modules

	$\nu$	$E_{\max}$ (N/m <sup>2</sup> )	$K_{\max}$	$G_{\max}$
Glacial Till	0.3	$7.2 \cdot 10^8$	$6.0 \cdot 10^8$	$2.77 \cdot 10^8$
Sand and Gravel	0.3	$1.92 \cdot 10^8$	$1.6 \cdot 10^8$	$7.38 \cdot 10^7$
Clay	0.495	$1.0 \cdot 10^8$	$3.33 \cdot 10^9$	$3.34 \cdot 10^7$
Fill and Slag	0.3	$1.92 \cdot 10^8$	$1.6 \cdot 10^8$	$7.38 \cdot 10^7$

The non-altered input parameters for each material are summarised in Table 8

Table 8 Non-altered material parameters

	$\rho$ (kg/m <sup>3</sup> )	Porosity $\epsilon$ (-)	$c$ (N/m <sup>2</sup> )	$\phi$ (deg)
Glacial Till	1900	0.3	$10 \cdot 10^3$	40
Sand and Gravel	1800	0.2	$10 \cdot 10^3$	40
Clay	1600	0.3	$30 \cdot 10^3$	20
Fill and Slag	1900	0.4	$14 \cdot 10^3$	40

Table 9 Material parameters for the concrete pile

	$\rho$ (kg/m <sup>3</sup> )	$\nu$	$E$ (N/m <sup>2</sup> )
Concrete Pile	2400	0.3	$25 \cdot 10^9$

## Damping

To model the material damping in COMSOL Multiphysics, Rayleigh damping is used with input parameters of  $\alpha$  and  $\beta$ , see section 2.8.2. With the use of extreme values of frequency from the field test (8 and 15 Hz),  $\omega_1 = 2\pi \cdot 8$  and  $\omega_2 = 2\pi \cdot 15$ . With  $\zeta = 0.04$  according to damping spectra, see 2.8.2,  $\alpha$  and  $\beta$  are calculated as:

$$2\zeta_1\omega_1 = \alpha + \beta\omega_1^2 \quad (54)$$

$$2\zeta_2\omega_2 = \alpha + \beta\omega_2^2 \quad (55)$$

**Element size**

The element size for a simulation is of great importance. For a time dependent study COMSOL Multiphysics (2016) recommends that the mesh size equals the ratio between the wave speed in the medium,  $c_s$ , divided by the maximum frequency that is of significance multiplied by a number that expresses the number of mesh elements per wavelength,  $N$ . (COMSOL Multiphysics, 2016) The equation can be seen below

$$h_0 = c_s / (Nf_0) \tag{56}$$

Taken computation time into consideration the recommended element size will only be applied on the upper layers. The element distribution for the entire geometry is displayed in Figure 26.

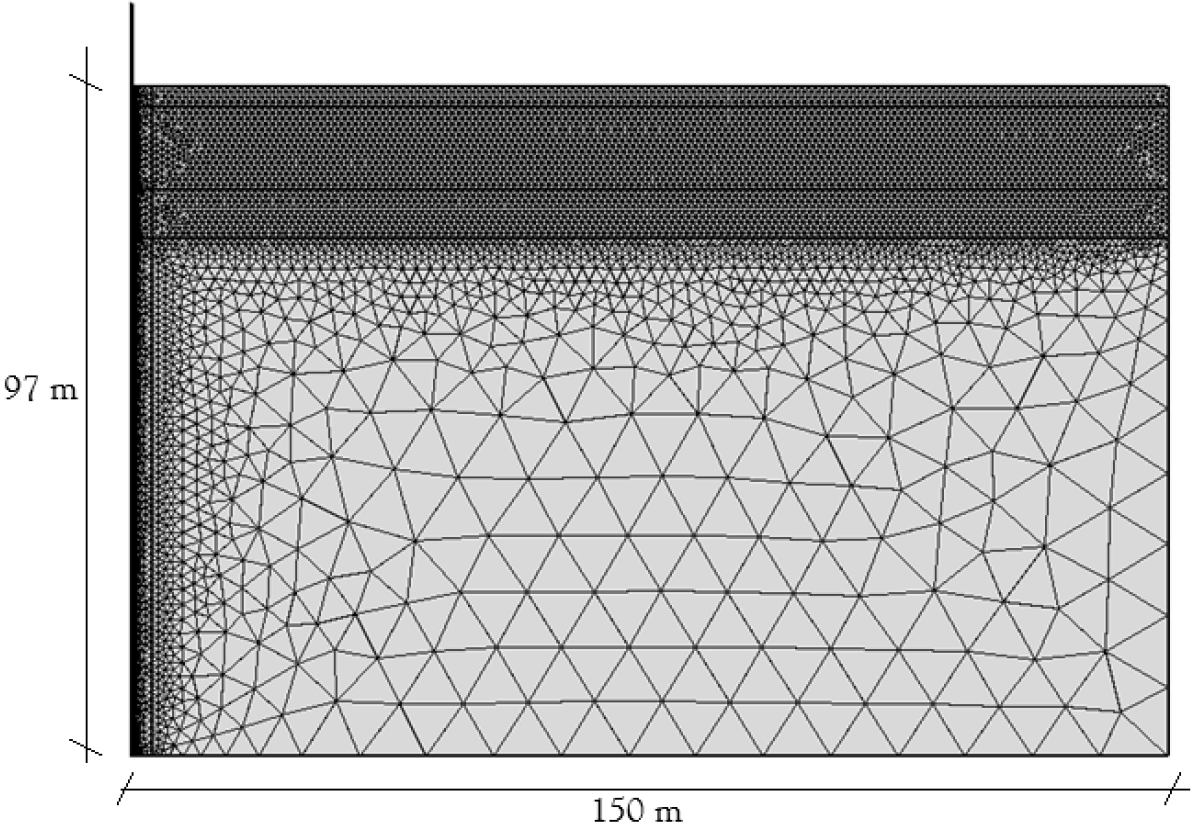


Figure 26 Mesh distribution for the entire geometry

The mesh distribution closer to the pile changes rather dramatically. The mesh distribution is therefore displayed in Figure 27. The maximum element size for this part is in accordance with eq. 56.

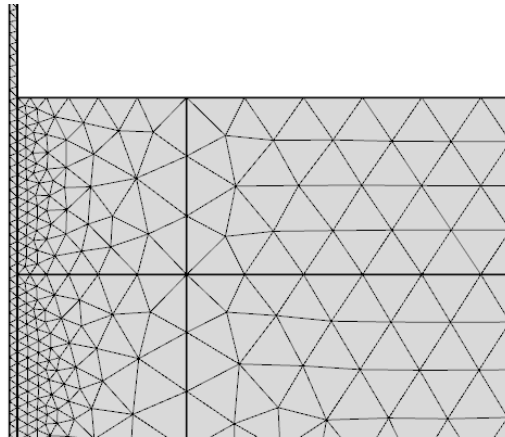


Figure 27 Mesh distribution in proximity to the pile

### Time steps

It is required that the time step at which the program COMSOL Multiphysics computes each step matches the size of the mesh. COMSOL Multiphysics (2016) recommends a maximum CFL number for the element size- time step as 0.2. The CFL number is computed as

$$\text{CFL} = c_s \Delta t / h \quad (57)$$

where  $c_s$  is the wave speed in the medium and  $h$  denotes the length on one side (COMSOL Multiphysics, 2016).

Due to computation difficulties with non-linear-models, it is required to use smaller time steps in order for the model to converge. A time step of one tenth of the recommended time step is used.

### 4.2.3 Study set up

The calculations in COMSOL Multiphysics have been divided into two steps. The first step is to find the initial stresses and strains in a soil considering gravity. The second step is where the impact from the pile installation is added. To decide at what time the steady state is reached, a parametric study is made. Alternation of the extreme values of Young's modulus is made to be compared with the field test results.

#### Study 1 - Gravity 0-1000s.

Consider the boundary that is marked with thick black in Figure 28. When this boundary has reached a steady state, the change in stress levels caused by the gravity is assumed to have stopped for the entire geometry.

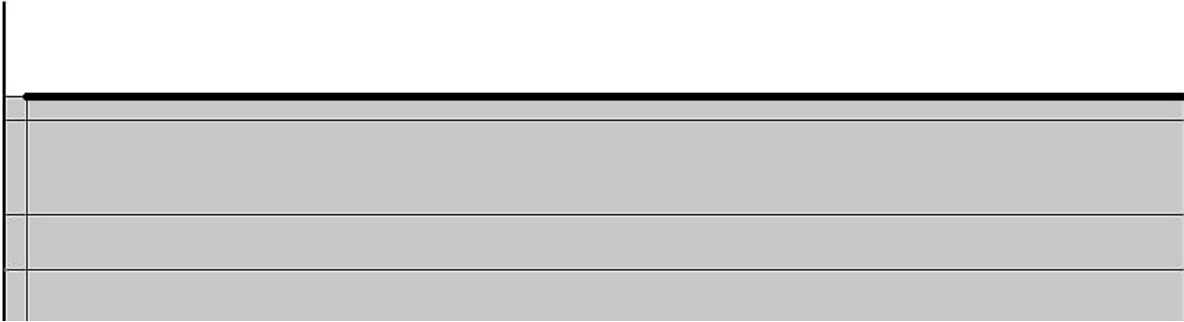


Figure 28 Boundary of interest

The displacements in the vertical direction for the boundary in Figure 28 are plotted against the time in Figure 29.

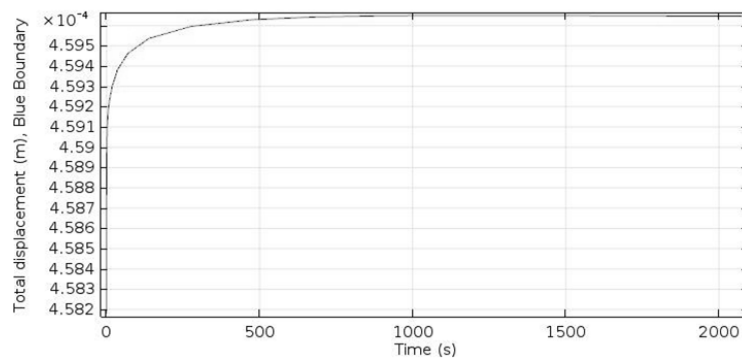


Figure 29 Displacement- time plot

As can be seen in Figure 29 the displacement alteration subsides and becomes constant at the time 1000s. As a conclusion the first time step will therefore be from 0 to 1000s.

## Study 2 - Hammer impact

The solution from the steady state analysis in Study 1 will be the initial values in Study 2. This means the soil has reached its steady state and has initial stresses in both vertical and horizontal directions. In Step 2, a time dependent study is made for the duration of 0.7 seconds. The hammer will impact at time 0.01s for a duration of 0.1 seconds, see 4.2.2. The particle velocities at the distances of interest are studied for the different values of Young's modulus.

## Chapter 5

# Results

In this chapter, the results from the simulations are presented. The results are presented as follows:

- Results from the steady state study
- Results of the wave propagation
- Results of the particle velocities

### 5.1 Steady State

The soil has been exposed to gravity during 1000 seconds to reach a steady state. This gives an initial stress state in the soil which gives an adequate soil stress representation for further studies. Figure 30 illustrates the stresses in the soil after reaching steady state for all the simulations. In the bottom of the geometry, the value of stress is significantly greater than the top, since the stress in both vertical and horizontal direction increases with depth, according to section 2.2.2. The figure illustrates the total stress, and not the effective stress, since the water table is not taken in consideration in the steady state.

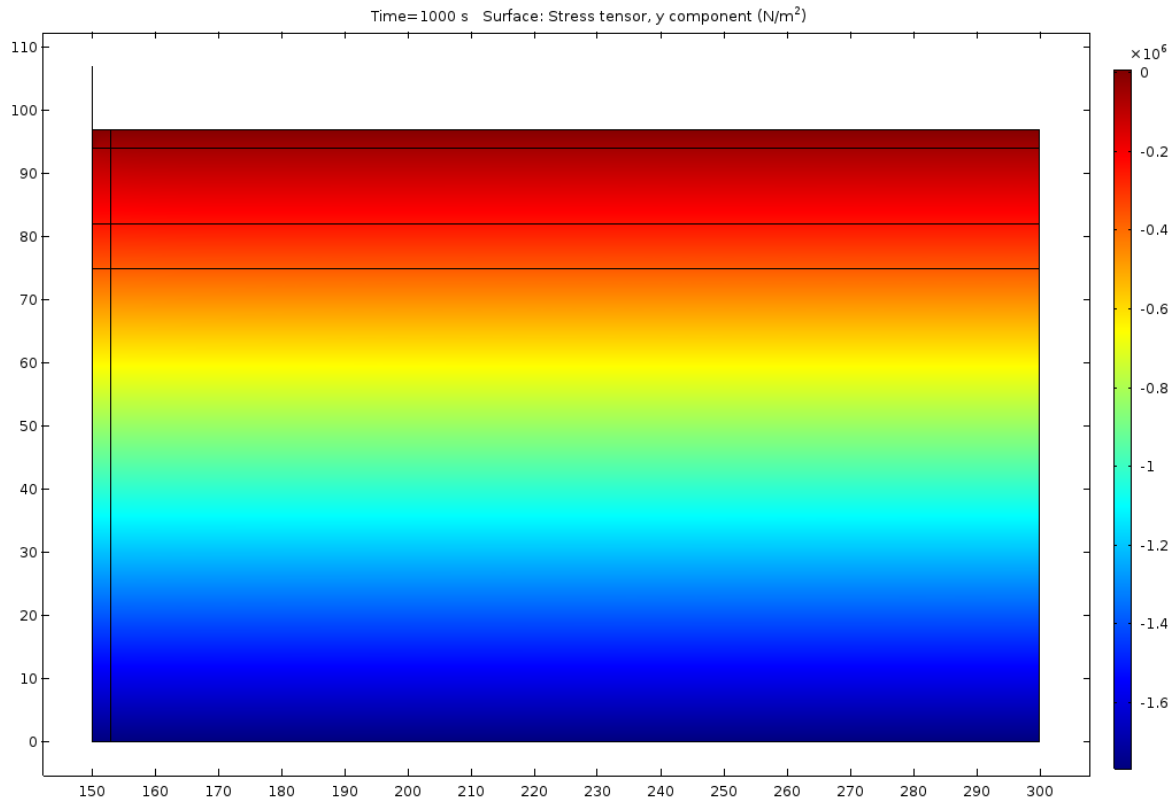


Figure 30 Steady state stress in the vertical direction after 1000 seconds.

## 5.2 Wave propagation

The figures in this section illustrate several plots of the wave propagation for the Drucker-Prager model with maximum Young's moduli for the soil layers. The wave propagation can be seen as it propagates over time. The elastic model and the Mohr-Coulomb model have great resemblance with the Drucker-Prager model regarding wave propagation, hence no illustrations of these are given below.

The wave propagation with lower values of Young's moduli have the same propagation pattern, but with a lower propagation velocity in unity with the equations in section 2.6. Therefore, these figures are not presented and the following presentation of figures is merely a general presentation of the wave propagations at different pile depths rather than an exact illustration for every material set up.

### 5.2.1 Pile depth 3 meters

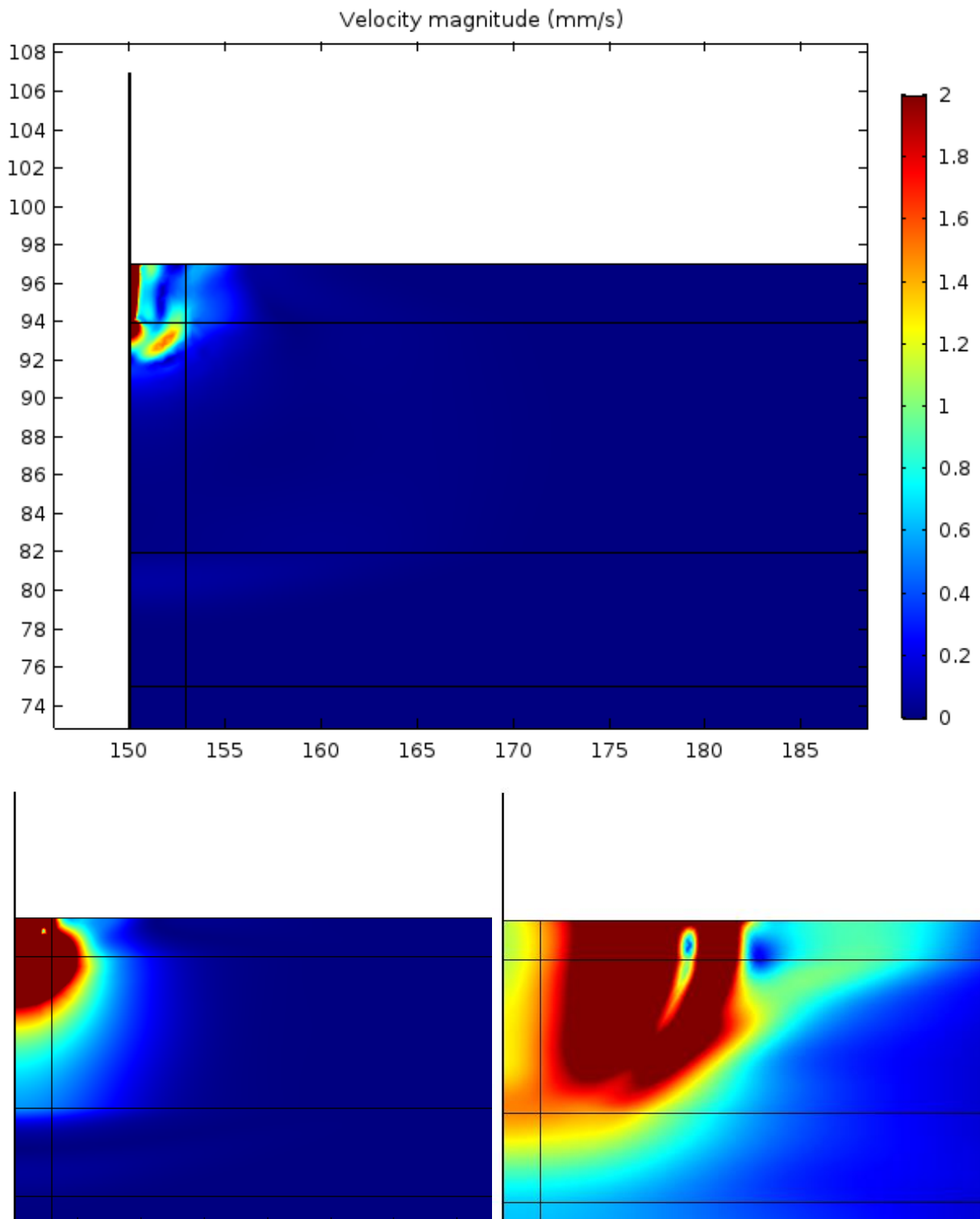
Figure 31 illustrates a selection of the wave propagation and particle velocity magnitude for the Drucker-Prager model. The figure illustrates the pile depth of 3 meters with the maximum value of Young's modulus, according to Table 6

In Figure 31, A), the impact load is initiated. It can be seen that along the pile shaft, the shear wave is generated. It can also be seen the pressure wave being generated at the pile toe, demonstrated in a sphere-shaped pattern.

In Figure 31,B) the wave propagation is illustrated during the impact. As can be seen, the faster pressure wave has overtaken the slower shear wave. This results in creation of a Rayleigh wave at the soil surface. On the other hand, the shear wave and the pressure wave still appear in the soil but since the figure only represents the velocity magnitude in an arbitrary direction, it can only be determined in one point, not determine whether it is a p or a s-wave.

In Figure 31, C), the pile is not subjected to any impact, hence no creation of waves from the pile installation occurs. The waves that have been created propagate in the soil with the higher velocity magnitudes of the particles staying in the top layers. The light shade of blue in the periphery of the figure indicates that the waves have propagated throughout the entire geometry.

Figure 31 Illustration of wave propagation with the Drucker-Prager material model at pile depth 3 meters. A)Top: Impact initiation,  $t=0.0142s$ . B)Bottom left: during impact,  $t=0.0263s$ . C)Bottom right: Wave propagation after impact,  $t=0.1532s$



### 5.2.2 Pile depth 11.5 meters

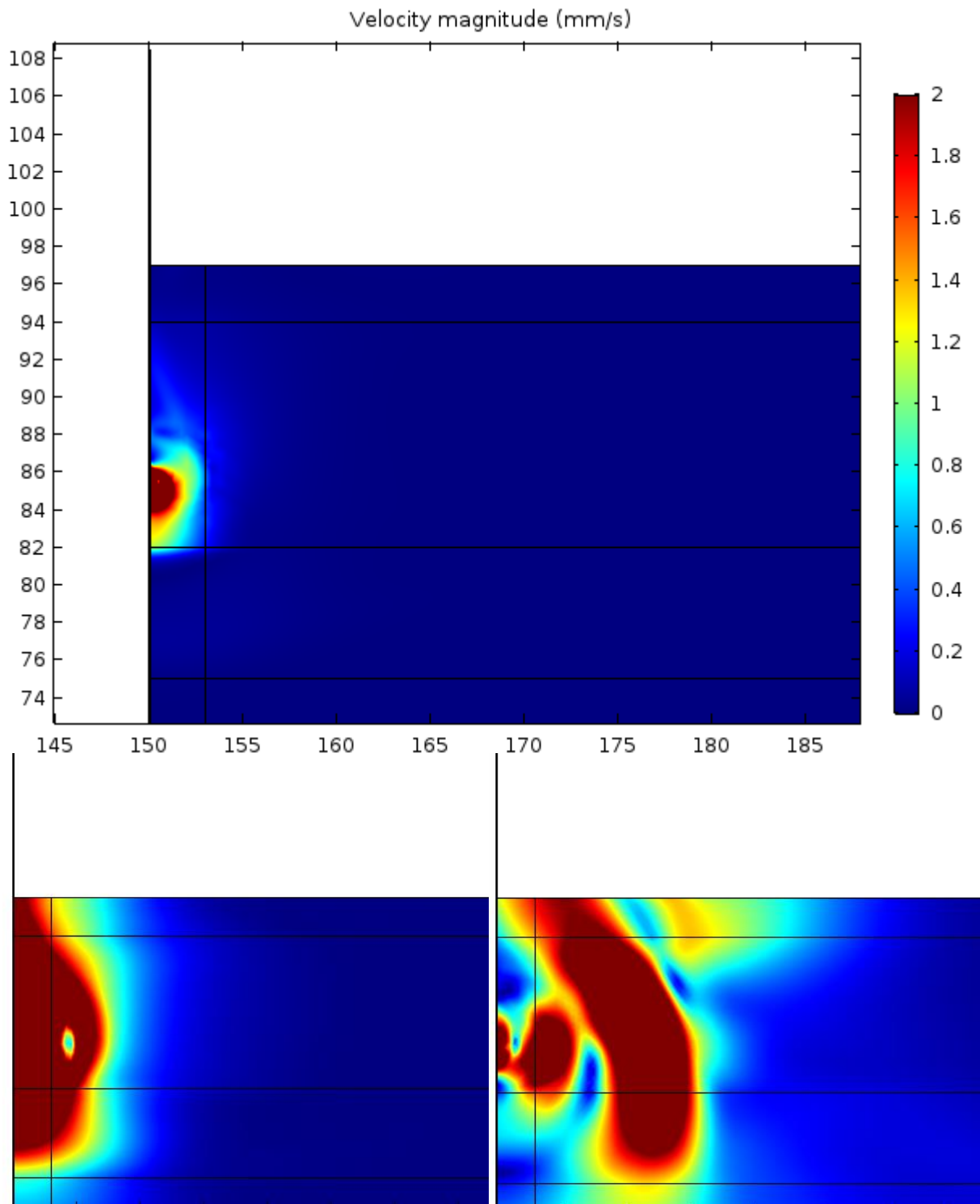
Figure 32 illustrates a selection of the wave propagation and particle velocity magnitude for the Drucker-Prager model. The figure illustrates the pile depth of 11.5 meters with the maximum value of Young's modulus, according to Table 6.

In Figure 32, A), the impact load is initiated. In distinction with Figure 31, no explicit indication of a creation of a shear wave along the pile shaft can be seen. The shear wave has not yet been generated since the spring along the pile shaft has a lower stiffness than the spring in the bottom of the pile, i.e. the resistance in the shaft has not yet been mobilised. It can also be seen the pressure wave being generated at the pile toe, demonstrated in a sphere-shaped pattern.

In Figure 32, B), the wave propagation is illustrated during the impact. The shear wave has now been generated, as can be seen along the pile shaft. Since the pile is on a depth of 11.5 meters instead of 3 meters, the pressure wave has not yet reached the surface and no explicit interaction of the shear wave and the pressure wave can be seen. This implies that the Rayleigh wave creation has only started.

In Figure 31, C), the pile is not subjected to any impact. At the pile toe, vibration is still occurring. The pressure wave propagates in a spherical pattern, typical for the pressure wave. Because of the geometrical damping when the pressure wave propagates, the amplitude decreases with the distance from the pile toe. Although the pressure wave is propagating spherically, the greatest value of the vibration magnitude of the particles appears in the upper layers. These materials have a lower Young's modulus and are less dense due to the initial stress state.

Figure 32 Illustration of wave propagation with the Drucker-Prager material model at pile depth 11,5 meters. A)Top: Impact initiation,  $t=0.0142s$ . B) Bottom left: during impact,  $t=0.047s$ . C)Bottom right: Wave propagation after impact,  $t=0.1628s$



### 5.2.3 Pile depth 17 meters

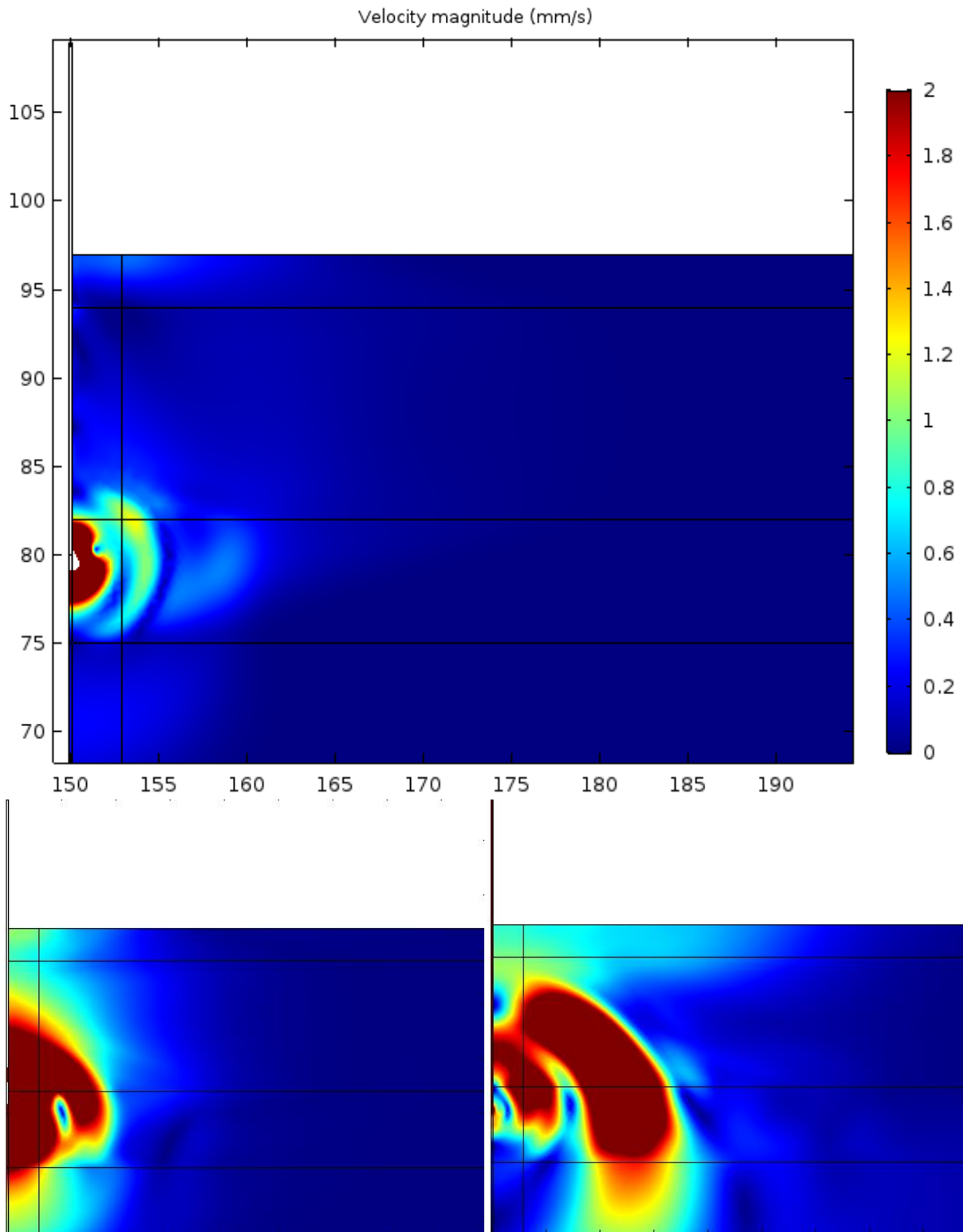
Figure 33 illustrates a selection of the wave propagation and particle velocity magnitude for the Drucker-Prager model. The figure illustrates the pile depth of 17 meters with the maximum value of Young's modulus, according to Table 6.

In Figure 33, A), the impact load is initiated. The wave propagation is similar to the propagation in Figure 32.

In Figure 33, B), the wave propagation is illustrated during the impact. The shear wave has now been generated, as can be seen along the pile shaft. Since the pile is on a depth of 17 meters instead of 3 or 11.5 meters, the pressure wave has not yet reached the surface and no explicit interaction of the shear wave and the pressure wave can be seen. This implies that the Rayleigh wave creation has only started.

In Figure 33, C), the pile is not subjected to any impact. The behaviour of the wave propagations are the same as in Figure 32 C). The pressure wave has not yet reached the surface of the soil. This implies that the light blue colour at the surface must either be the Rayleigh wave or the shear wave.

Figure 33 Illustration of wave propagation with the Drucker-Prager material model at pile depth 17 meters. A)Top: Impact initiation,  $t=0.0236s$ . B) Bottom left: during impact,  $t=0.0446s$ . C) Bottom right: Wave propagation after impact,  $t=0.1532s$



## 5.3 Particle velocities

In this section of the chapter the results from the vertical particle velocities at the different horizontal distances are presented. Figure 34 illustrates the arrangement of the probe points in the field test. These points are also the points from where the vibrations are extracted in the FE-model.

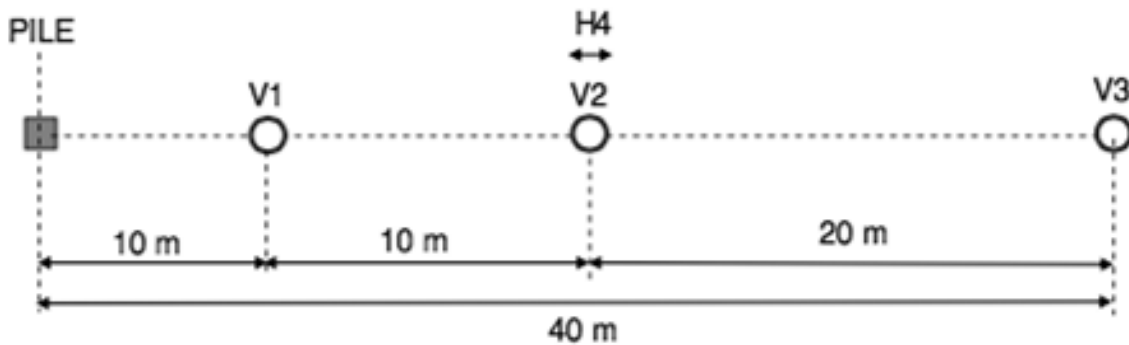


Figure 34 Arrangement of vibrations sensors during driving of the test pile. V1, V2 and V3 indicate vertical geophones and H4 indicate horizontal geophone. (Massarsch & Fellenius, 2008). These probe points are also the points from where the vibrations are extracted in the FE-model.

For every simulation a corresponding particle velocity graph is presented. The graphs show the extracted values of particle velocity during a time interval of 0.7 seconds. This interval represents the time for a single hammer impact with additional time for the waves to propagate. The graphs are presented in a way to easily make a comparison between the different models and Young's moduli. For comparison with the field test made by Nilsson in 1989, the graphs from these tests are presented in connection with the results from the simulations. For the pile depths of 3 meters, all the probe points in Figure 34 are presented. For pile depths of 11.5 and 17 meters only probe points of V2 and H4 are presented. This is due to the execution of the field test, where only results from V2 and H4 are available. On the following pages, results from the simulations can be seen. In Figure 35 to Figure 38 the results from the simulations with a pile depth of 3 meter can be seen. In Figure 39 and Figure 40 the simulations with a pile depth of 11.5 meter are presented. In Figure 41 to Figure 42 results from simulations with a pile depth of 17 meter are shown. The reader is asked to observe the amplitudes of the vibrations and the shape of the graphs and compare it to the field test. A comparison between the different material models and modules can also be done.

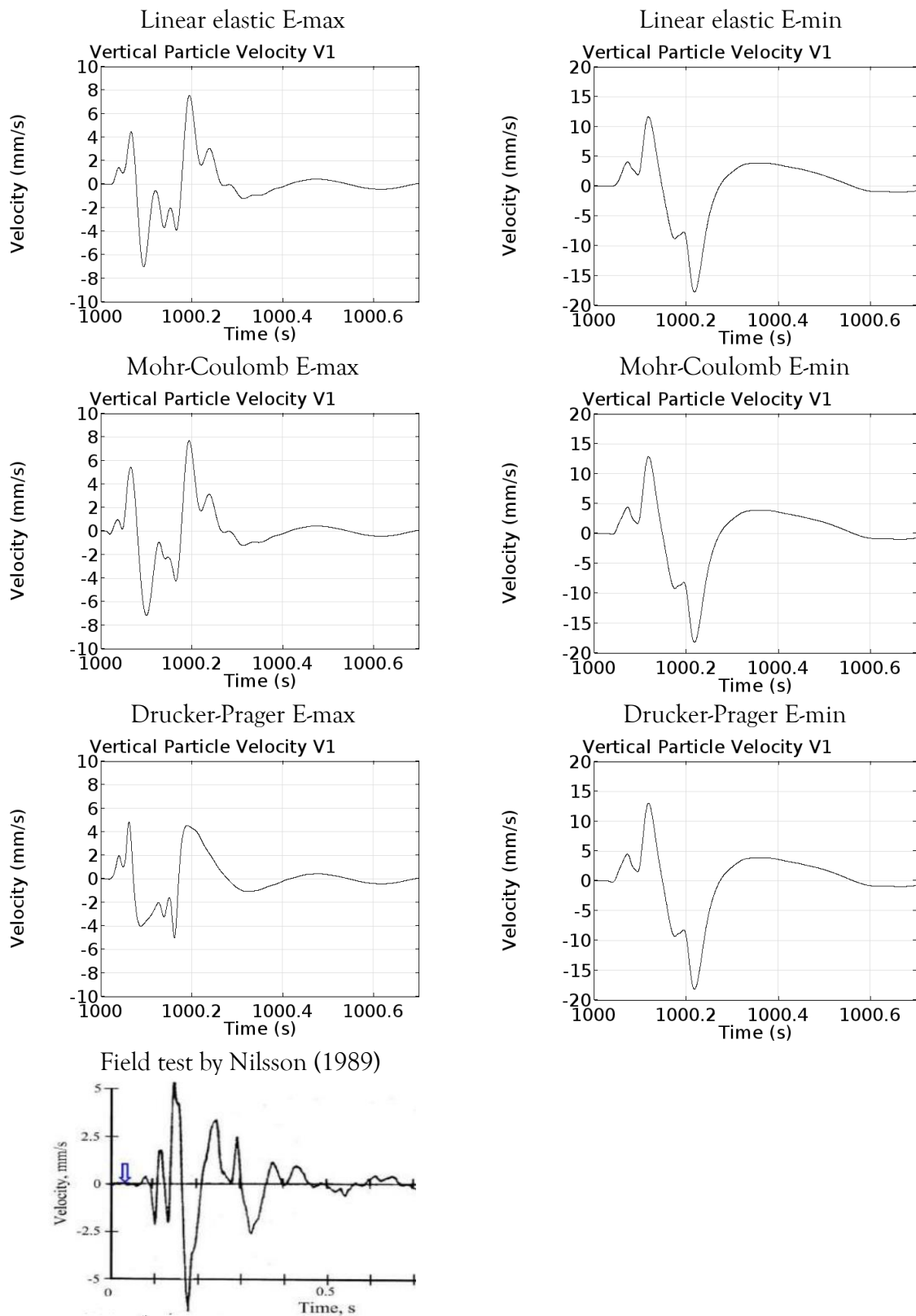


Figure 35 Pile depth 3 meters. Velocity graphs at probe point V1. E-max in the left column, E-min in the right column. Elastic, Mohr-Coulomb and Drucker-Prager are presented. Field test measurement in the bottom.

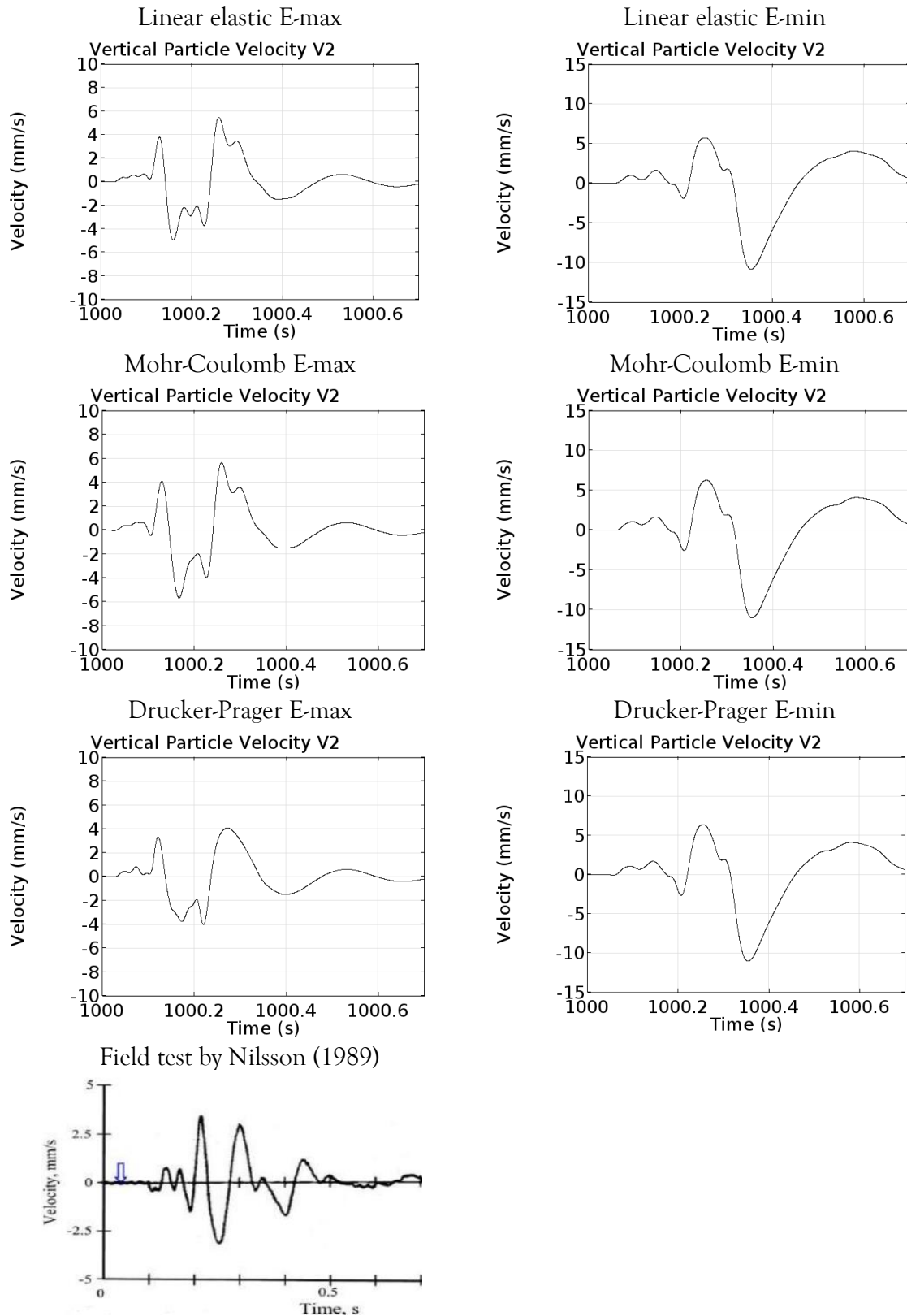


Figure 36 Pile depth 3 meters. Velocity graphs at probe point V2. E-max in the left column, E-min in the right column. Elastic, Mohr-Coulomb and Drucker-Prager are presented. Field test measurement in the bottom.

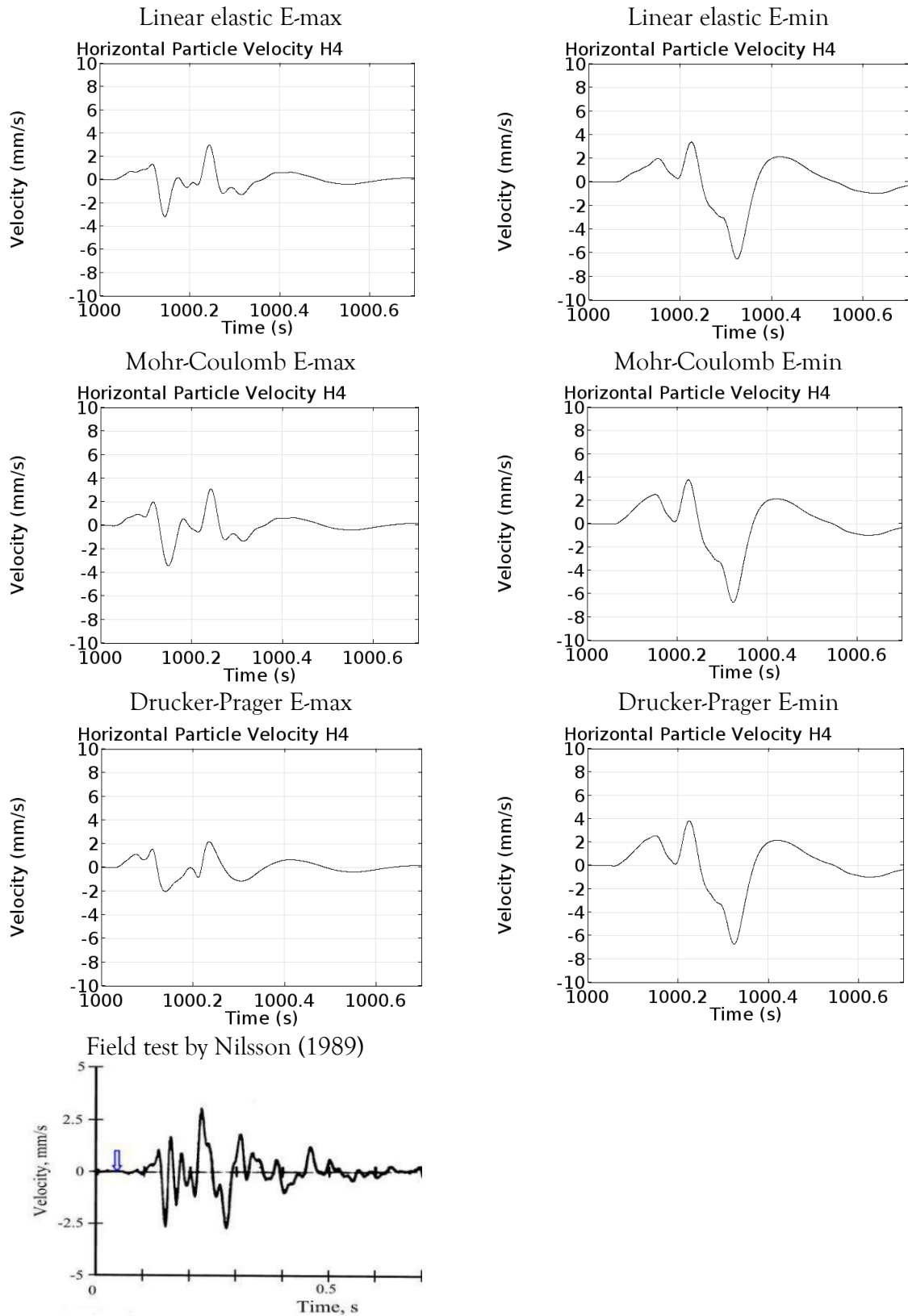


Figure 37 Pile depth 3 meters. Velocity graphs at probe point H4. E-max in the left column, E-min in the right column. Elastic, Mohr-Coulomb and Drucker-Prager are presented. Field test measurement in the bottom.

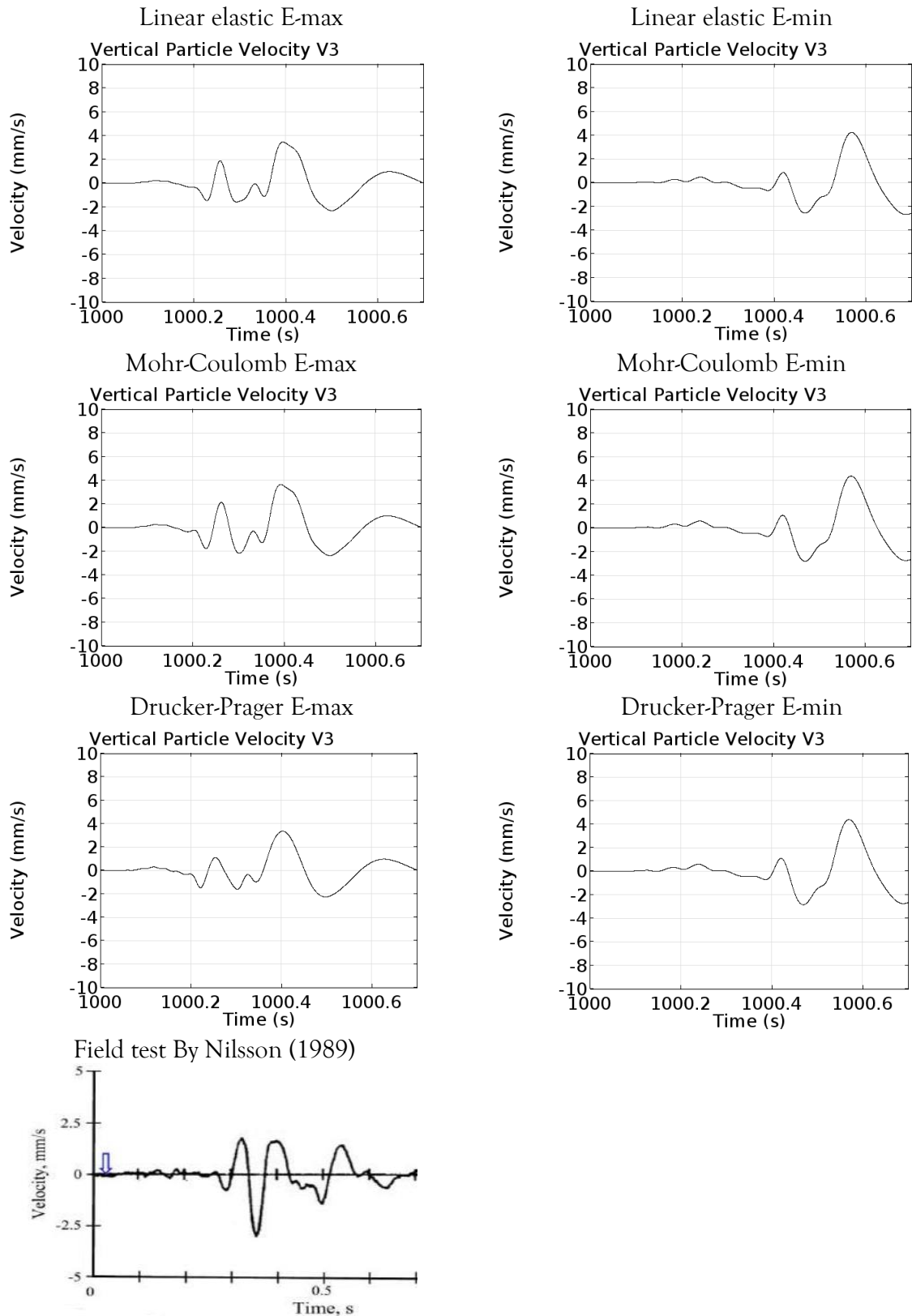


Figure 38 Pile depth 3 meters. Velocity graphs at probe point V4. E-max in the left column, E-min in the right column. Elastic, Mohr-Coulomb and Drucker-Prager are presented. Field test measurement in the bottom.

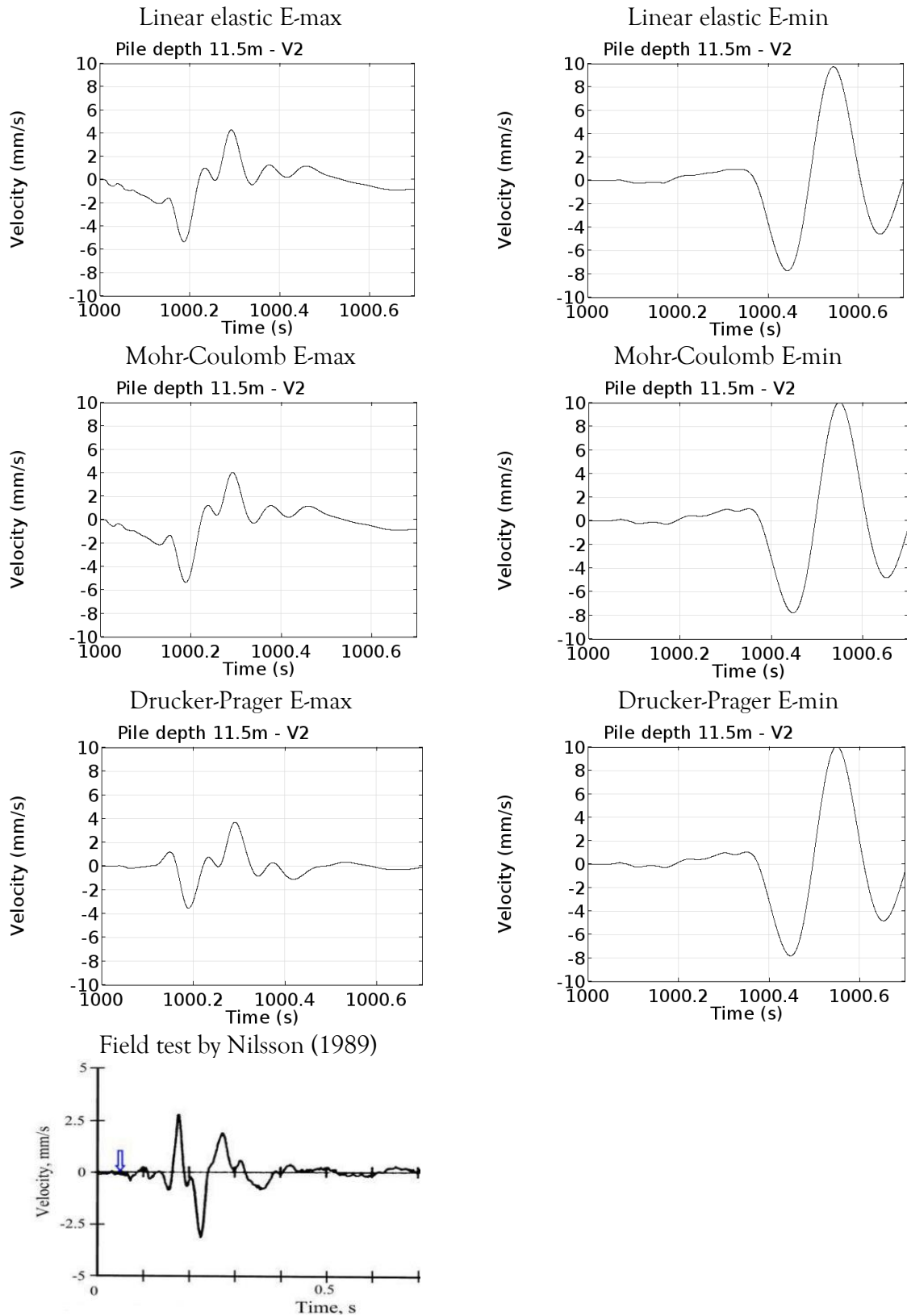


Figure 39 Pile depth 11.5 meters. Velocity graphs at probe point V2. E-max in the left column, E-min in the right column. Elastic, Mohr-Coulomb and Drucker-Prager are presented. Field test measurement in the bottom.

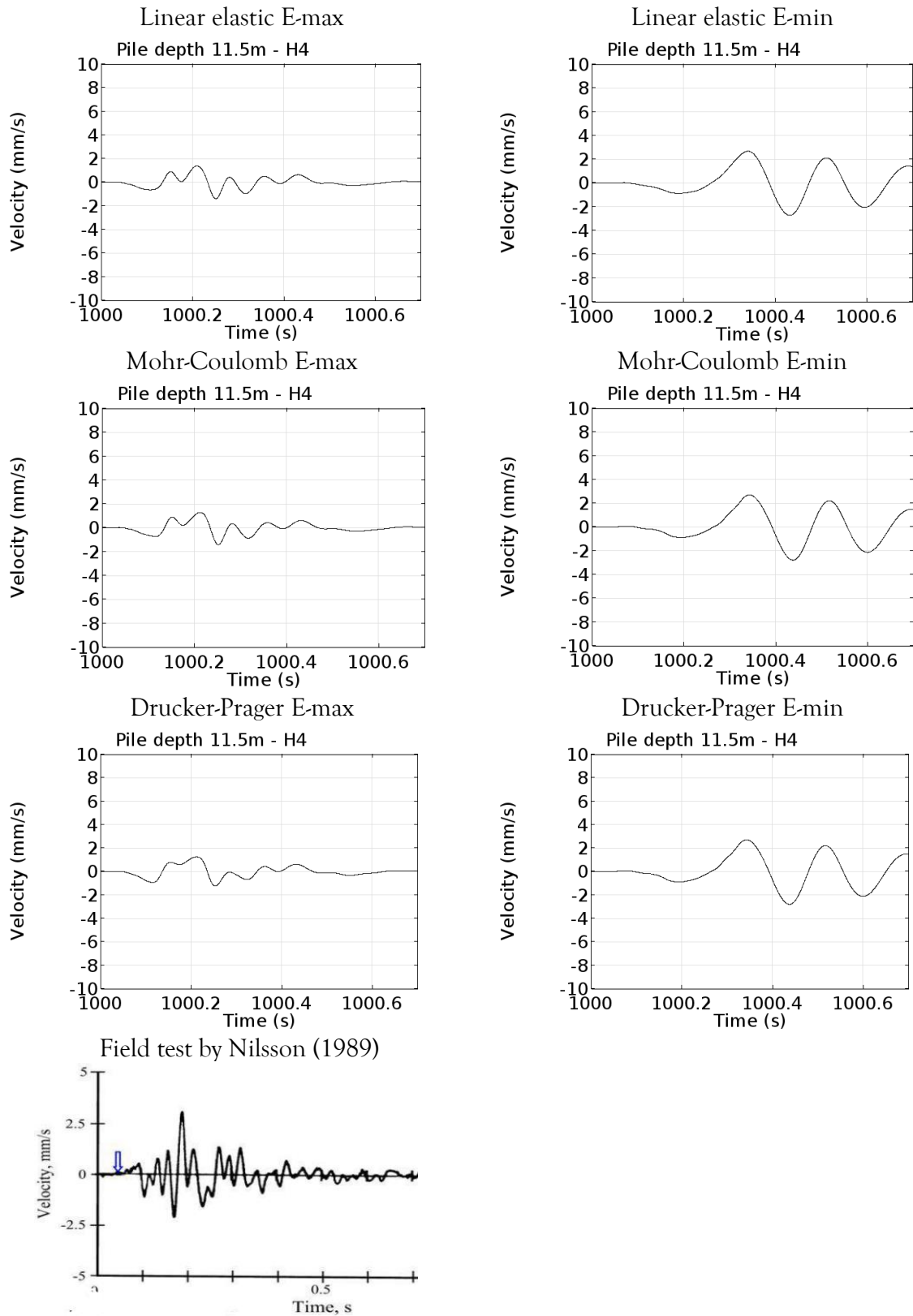


Figure 40 Pile depth 11.5 meters. Velocity graphs at probe point H4. E-max in the left column, E-min in the right column. Elastic, Mohr-Coulomb and Drucker-Prager are presented. Field test measurement in the bottom.

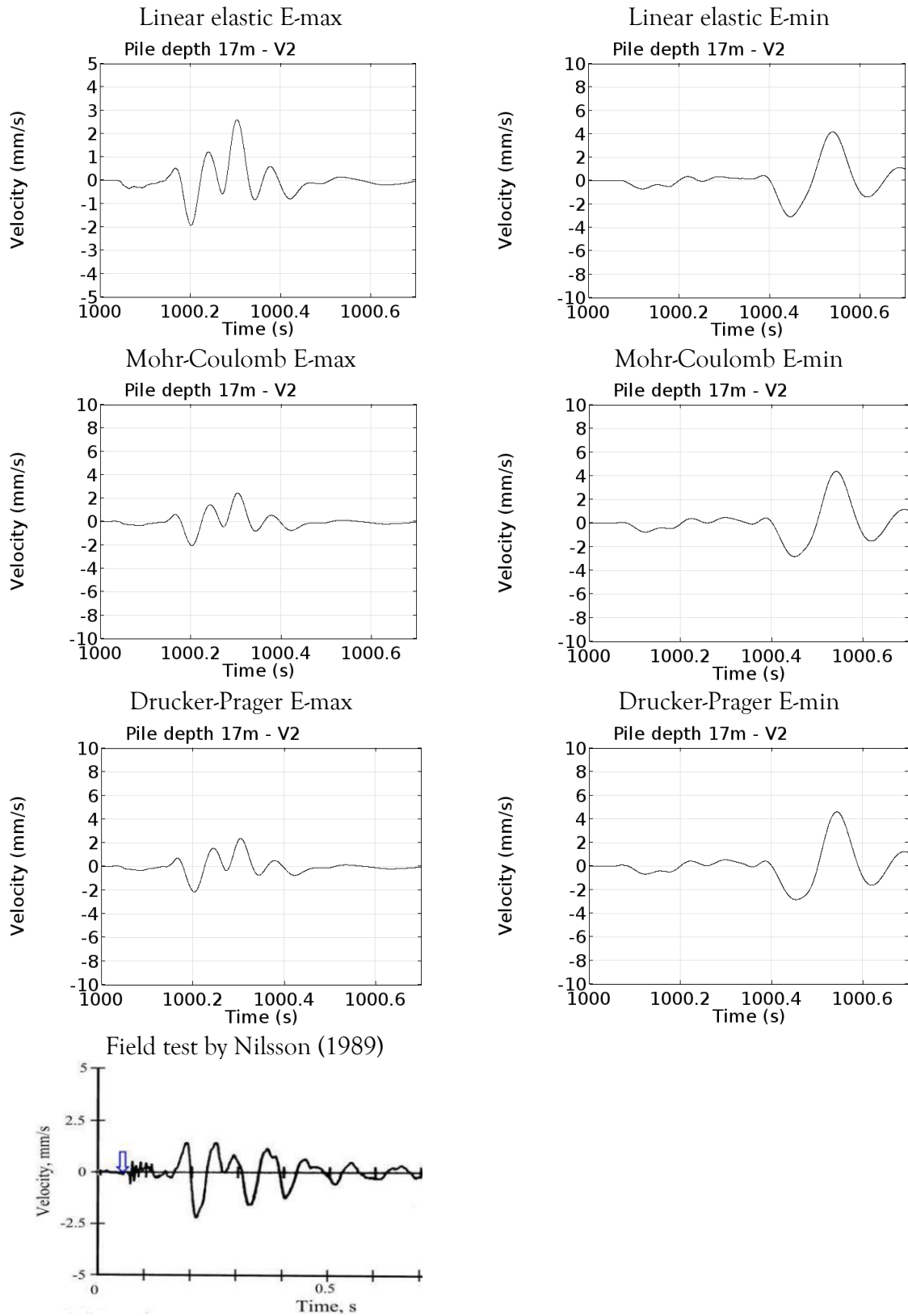


Figure 41 Pile depth 17 meters. Velocity graphs at probe point V2. E-max in the left column, E-min in the right column. Elastic, Mohr-Coulomb and Drucker-Prager are presented. Field test measurement in the bottom.

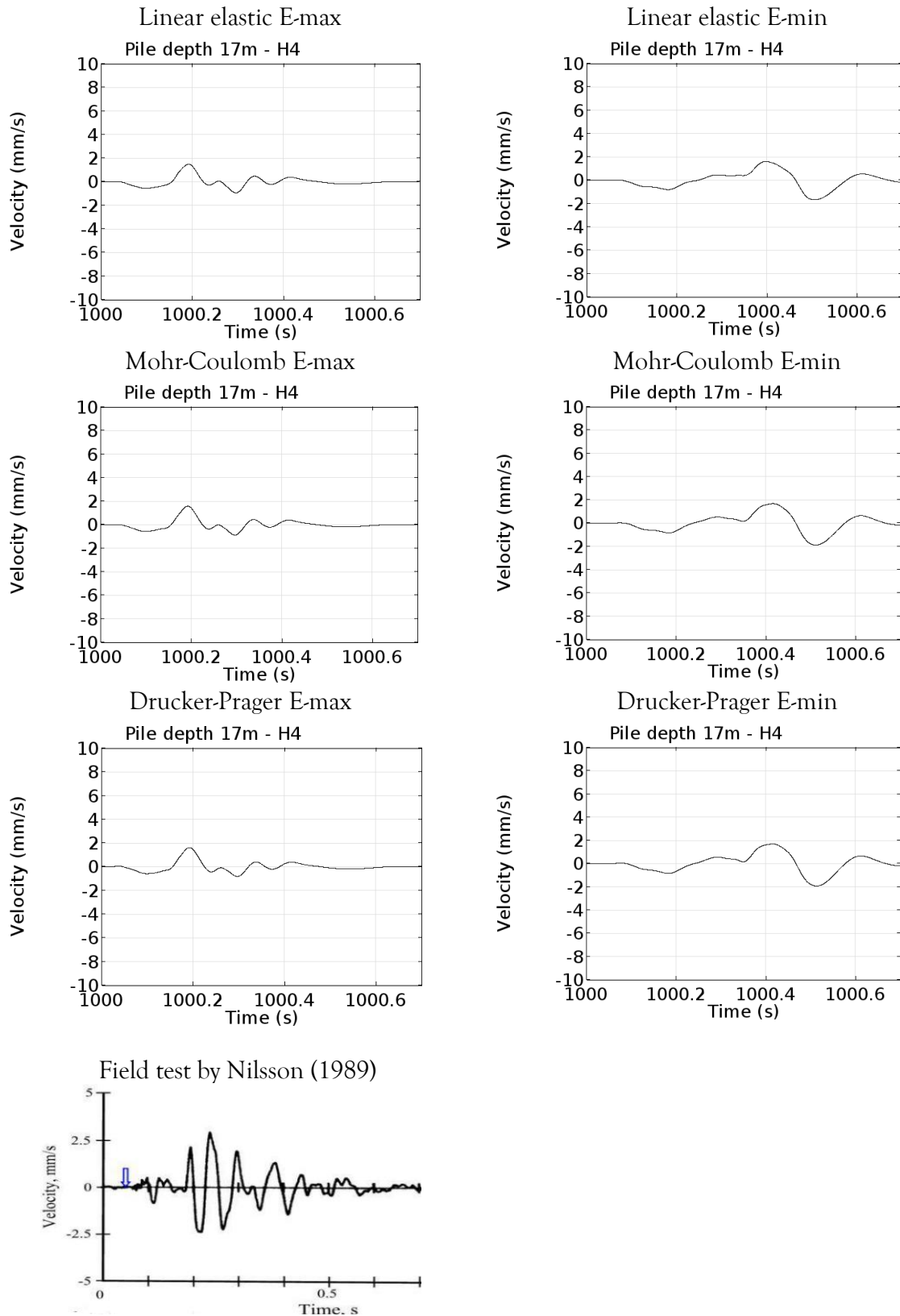


Figure 42 Pile depth 17 meters. Velocity graphs at probe point H4. E-max in the left column, E-min in the right column. Elastic, Mohr-Coulomb and Drucker-Prager are presented. Field test measurement in the bottom.



## Chapter 6

# Discussion and Conclusion

In this chapter, the results are analysed and discussed. The analysis is done based on the objection formulation and a comparison with the field test result is made. Error sources and suggestions for further studies are also presented.

## 6.1 Discussion

### 6.1.1 Young's modulus and vibrations

The altering of Young's modulus gives changes to the bulk modulus and shear modulus as well, according to section 2.2.2. The effect of the altering gives a significant difference in the vibrations, expressed in particle velocity. This difference can be seen in each comparison of the extreme values of Young's modulus for each pile depth. This confirms the effect of Young's modulus and Poisson's ratio in the equation of wave propagation of the pressure wave, eq. 28.

For every comparison of the extreme values of Young's modulus, the time offset is delayed for the models with the lower modulus. On the other hand, a lower modulus gives a greater value of the vibration. This means that with a greater value of Young's modulus, the wave propagates at a faster rate but with a lower amplitude. Young's modulus represents a relationship between stress and strain. Since a low modulus represents more strain for a given stress than a situation with a great value of the modulus, this leads to a greater strain, or deformation, and therefore also a greater amplitude.

Even though not presented in the results, the ppv could be extracted from the simulations since it is a resultant of the particle velocities in every direction. The ppv is often a vibration of interest while designing structures since the resultant is the absolute value, and vibrations can damage structures. The object of this work is not to extract the ppv, but trying to make a model to simulate vibrations. This can further more be used as a tool to predict vibrations such as ppv.

### 6.1.2 Material models

Three material models have been studied. One linear elastic and two plastic models. The two plastic models are set up with the Mohr-Coulomb yield criterion and the Drucker-Prager yield criterion respectively. The soil in all the models are assumed to be isotropic. The two models have an identical setup with the soil close to the pile having the possibility to plastically deform, while the rest of the soil in the models have elastic properties.

When comparing the two plastic models, few variations are found. There are small behavioural differences of the amplitude propagation, but the peak values of the amplitudes are all in the same magnitude for the two models. This applies for both the maximum and minimum values of Young's modulus.

When comparing the two plastic models with the elastic model, differences are found. For pile depth of 3 meters plastic response can be seen for both the Mohr-Coulomb and the Drucker-Prager models. The greatest discrepancies are found in the Drucker-Prager model when compared with the elastic model. For the other pile depths, no significant discrepancies between the models were found. For the pile depth of three meters, the pile toe is as close to the measuring points as possible which means the wave has to travel the shortest way compared with the other pile depths. It may be possible that the different material models would be of greater importance if the stresses and deformations are studied during a whole pile installation – from start to end.

One reason the results tend to have a lower magnitude in the Drucker-Prager models can be how the yield criterion is set up. In this study, the circle of the Drucker-Prager yield surface is constructed so that it is fitted inside the Mohr-Coulomb yield surface, hence these reaches a plastic state sooner than the Mohr-Coulomb models. This may lead to less energy propagating from the pile toe where the greatest stress occurs.

### 6.1.3 Comparison with Field test

Regarding the higher Young's modulus some resemblance can be seen with the field test by Nilsson (1989). At the pile depth of 3 meter all the three material models generates a graph that has an absolute maximum particle velocity that are within acceptable limits from the field test.

The graphs generated with the lower value of Young's modulus does hardly have any resemblance with the field test made by Nilsson (1989). Consequently they will not be discussed in this section.

Since the maximum particle velocity, rather than the wave form itself is of interest, this implies that with right composition of the material parameters for the soil layers one can accurately simulate vibrations and wave propagations with this FE-model.

### 6.1.4 Error sources

Error sources regarding the field are discussed in the report by Nilsson (1989)

There are several possible error sources in both the field test and in the finite element simulations. To begin with, the soil distribution that is considered in this report are an idealisation and may differ from the actual field conditions which are not known in detail. This fact alone can interfere a lot with the accuracy of the simulations.

The simulations have only been done in a 2D environment. In a 3D environment such as the field test the results may differ.

Due to convergence problems in the finite element software an approximation had to be made in the contact between the pile and soil. Instead of a contact that might have been more accurate, a thin elastic layer had to be used. Even though the spring stiffness's were calculated from the equations in section 2.3 this might not be the absolute truth.

The ground water table was not taken into regard in the simulations. This results in that the voids in the soil are considered to be "empty". Neither the pressure wave nor the shear wave can travel through empty voids. This might imply that the vibrations at the surface would be a bit altered if the ground water had been included in the model.

In the parameter study that was executed regarding the Young's modulus, the greatest and the lowest values were only performed with a maximum and minimum value for all the soil layers. This does not take into account that in fact there might be a mixture of Young's modulus, low in one layer and great in another, which might give the optimised vibration set up. Instead, this study can be seen as an illustration of the effects of the Young's modulus.

In this report the hammer blow has been simulated as a rectangle function. Due to lack of information regarding a real hammer impact function, the rectangle function is a simplification for describing the fast loading and unloading.

Due to saving on computational time the boundary conditions used in the simulations are not non-reflecting. This can affect the vibrations at the surface since especially the faster pressure wave can be reflected on the boundaries and interfere with the waves that are generated at hammer impact.

## 6.2 Conclusion

In this report, the lack of soil properties and parameters has still led to a result that resembles the field test.

A conclusion is that with accurate material properties and parameters for a given situation, the vibrations and wave propagations due to pile driving can be computed in a realistic way using a finite element software.

Some differences were found in the Drucker-Prager yield criterion and the Mohr-Coulomb yield criterion simulations in comparison with the elastic model.

The possibility to make vibration- and wave computations with a FE-model can be an efficient tool for predicting vibrations and wave propagation. Hence, this makes the FE-model to be a complement to field tests if accurate soil properties and piling conditions are at hand.

## 6.3 Further studies

- This study is carried out with a single hammer blow. Interesting studies would be the effect on the vibrations if repetitive blows were to be studied and how these vibrations would interfere.
- It could also be of interest to focus on how to compute settlements due to vibrations while installing a pile. Doing a fracture mechanics computation when the vibrations can be studied from start until end of a pile installation process.
- An interesting study would be to determine how the different soil parameters affect the vibrations and wave propagation in a FE-model.
- Compare with another field test to verify the approach used in this report.
- A study with friction contact between the pile and the soil instead of using a thin elastic layer.
- A study of the influence in the vibrations and wave propagation due to existing pile groups and structures in the soil.

# Bibliography

- Adejumo, T. W. (2013). *Installation techniques of pile foundation on some low bearing capacity soils in Nigeria*. Minsk: Department of Geotechnics and Environmental Engineering, Faculty of Civil Engineering, Belarussian National Technical University.
- Alejano, L. R., & Bobet, A. (2012). *Drucker-Prager Criterion*. Vigo, Spain and West Lafayette, USA: Springer-Verlag.
- Ascalew, A., & Smith, D. I. (2007). *Pile Foundation Design: A Student Guide*. Edinburgh: School of the Built Environment, Napier University.
- Atkinson, J. (2016, February 27). *Stiffness*. Retrieved from Basic Mechanics of Soils: <http://environment.uwe.ac.uk/geocal/SoilMech/basic/soilbasi.htm#BASICMECH>
- Austrell, P.-E. (2016, januari 19). *Institutionen för Byggnadsmekanik LTH*. Retrieved februari 27, 2016, from Byggnadsmekanik LTH: <http://www.byggmek.lth.se/utbildning/kurser/vsmn10-strukturdynamiska-beraekningar/>
- Baecher, G. (2015). D. W. Taylor and the Foundations of Modern Soil Mechanics. *Journal of geotechnical and geoenvironmental engineering - February*, 5-8.
- Bartlett, S. F. (2012). *Mohr Coulomb Model*. Bartlett.
- COMSOL. (2012). *COMSOL Multiphysics Reference Guide*. COMSOL.
- COMSOL Multiphysics. (2016, April 11). *Resolving time-dependent waves*. Retrieved from COMSOL Support: <https://www.comsol.com/support/knowledgebase/11118/>
- Cornfield, G., Haswell, C., & Burland, J. (1973). Prediction of Load Carrying Capacity of Piles. *Proceedings of the Institution of Civil Engineers Part 1 - Design and Construction*, 753-755.
- Deckner, F. (2013). *Ground vibrations due to pile and sheet pile driving - influencing factors, predictions and measurements, Licentiate thesis*. Stockholm: Royal Institute of Technology, KTH.
- Emdal, A., Grande, L., & Nordal, S. (2015). *Geoteknikk - Beregningsmetoder*. Trondheim: Faggruppe for Geoteknikk ved Norges teknisk-naturvitenskaplige universitet .
- EmecaSpe-USA. (2016, April 7). *Technical info*. Retrieved from Emeca Spe USA: <http://www.emeca-speusa.com/>
- Fossum, A. F., & Fredrich, J. T. (2000). *Cap plasticity models and compactive and dilatant pre-failure deformation*. Albuquerque, New Mexico: Sandia National Laboratories.
- Freeze, A., & Cherry, J. (1979). *Groundwater - 2nd Edition*. Upper Saddle River, NJ, USA: Prentice Hall, Inc.

- Hall, L; Wersäll, C. (2013). *SGF Informationsskrift 1:2012*. Göteborg och Stockholm: Svenska Geotekniska Föreningen.
- Hintze, S., Liedberg, S., Massarsch, R., Hanson, M., Elvhammar, H., Lundahl, B., & Rehnman, S.-E. (1997). *Omgivningpåverkan vid pål- och spontslagning*. Pålkommissionen. Linköping: Pålkommissionen.
- IEG. (2010). *IEG Rapport 12:2010*. Stockholm: Implementeringskommissionen för Europastandarder inom Geoteknik.
- Info, G. (2012). *Young's modulus of soil*. Retrieved from geotechnicalinfo.com: [http://www.geotechnicalinfo.com/youngs\\_modulus.html](http://www.geotechnicalinfo.com/youngs_modulus.html)
- Kramer, S. L. (1996). Wave Propagation. In S. L. Kramer, *Geotechnical Earthquake Engineering* (pp. 143-180). Upper Saddle River: Prentice-Hall.
- Labuz, J. F., & Zang, A. (2012). *Mohr-Coulomb Failure Criterion*. Patsdam and Minneapolis: Springer-Verlag.
- Landstreet, J. (2009, February 9). *Planets*. Retrieved from Astronomy and Astrophysics: <http://www.astro.uwo.ca/~jlandstr/planets/webfigs/earth/images/waves.gif>
- Lin, C. P. (2013). Chapter 3 - Rayleigh Waves. In C. P. Lin, *Multistation methods for geotechnical characterization using surface waves* (pp. 27-58). Hsinchu, Taiwan: National Chiao Tung University.
- Massarch, K., & Wersäll, C. (2014). Horisontell jordundantängning vid påslagning i lera. *Bygg och Teknik*, 46-51.
- Massarch, R., & Fellenius, B. (2013). *SGF Informationsskrift 1:2012 Markvibrationer*. Göteborg och Stockholm: Svenska Geotekniska Föreningen.
- Massarsch, R. K., & Fellenius, B. H. (2008). Ground Vibrations Induced by Impact Pile Driving. *The Sixth International Conference on Case Histories in Geotechnical Engineering*, (pp. 1-38). Arlington, VA.
- Möller, B., Larsson, R., Bengtsson, P.-E., & Moritz, L. (2000). *Geodynamik i praktiken, Information 17*. Linköping: Statens Geotekniska Institut.
- Nilsson, G. (1989). *Markvibrationer vid påslagning*. Stockholm: Jord- och bergmekanik vid institutionen för byggvetenskap vid KTH.
- Ortiz, M., & Pandolfi, A. (2004). *A variational Cam-clay theory of plasticity*. Pasadena, USA and Milano, Italy: Science Direct.
- Ottosen, N. S., & Petersson, H. (1992). *Introduction to the finite element method*. Essex: Pearson Education Limited.
- Pålkommissionen. (2007). *Pålgrundläggning, Grundinformation för projektörer, Information 2007:1*. Pålkommissionen.

- Rausche, F. (2000). Pile driving equipment: Capabilities and properties. *Proceedings of the Sixth International Conference on the Application of Stress Wave Theory to Piles* (pp. 75-89). Sao Paulo, Brazil: Goble Rausche Likens and Associates Incorporated.
- Reynolds, T. N. (2016, Mars 21). *Forestry Commision Home Page*. Retrieved from Publications: [http://www.forestry.gov.uk/pdf/crwoodproducts23.pdf/\\$FILE/crwoodproducts23.pdf](http://www.forestry.gov.uk/pdf/crwoodproducts23.pdf/$FILE/crwoodproducts23.pdf)
- RocScience. (2016, February 26). *Description of Cam-Clay and Modified-Cam-Clay Critical State Strength Models*. Retrieved from Rocscience: [https://www.rocscience.com/help/phase2/webhelp/pdf\\_files/theory/CamClay.pdf](https://www.rocscience.com/help/phase2/webhelp/pdf_files/theory/CamClay.pdf)
- Schofield, A. N. (1993). *Orginal CAM-CLAY*. Cambridge: Department of Engineering, University of Cambridge.
- SGU. (2016, February 5). *Från Istid till Nutid*. Retrieved Februari 19, 2016, from Sveriges Geologiska Undersökning: <http://www.sgu.se/om-geologi/jord/fran-istid-till-nutid/inlandsisen/moran-spar-av-inlandsisen/>
- Spetz, A. (2012). *Assesment of finite element softwares for geotechnical calculations*. Lund: Lund University.
- Sture, S. (2004). *Mohr-Coulomb Model - Short Course on Computational Geotechnics + Dynamics*. Boulder: Universiy of Colorado at Boulder.
- Terzaghi, K. (1986). *Terzaghi Lectures 1974-1982*. New York: American Society of Civil Engineers.
- Terzaghi, K., Peck, R. B., & Mesri, G. (1996). *Soil Mechanics in Engineering Practice - Third Edition*. New York, USA: John Wiley & Sons, Inc.
- Verruijt, A. (2012). *Soil Mechanics*. Delft: Delft University of Technology.
- Wood, D. M. (1990). Stress dilatancy. In D. M. Wood, *Soil behaviour and critical state soil mechanics* (pp. 226-255). New York: Cambridge University Press.
- Voyiadjis, G. Z., & Song, C. R. (2006). *The Coupled Theory of Mixtures in Geomechanics with Applications*. Amsterdam, The Netherlands: Springer-Verlag Berlin Heidelberg New York.

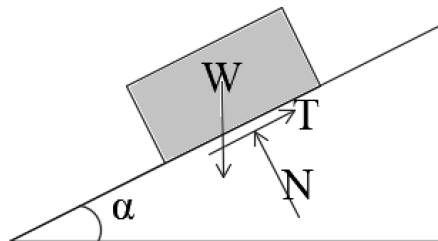


# Appendix

## A

### Coulomb criterion

Imagine a block that is situated on a slope as in Figure 43 below. It is easily obtained that the shear force equilibrium concludes  $T = W \sin \alpha$ , and the normal force equilibrium  $N = W \cos \alpha$ .



t

Figure 43 Block on slope (from (Verruijt, 2012))

The shear force and normal force equilibrium combined becomes  $T = N \tan \alpha$ . If both sides are divided by the length, stresses are obtained instead of forces.

In the late eighteenth century Coulomb added the cohesion constant,  $c$ , which made the formula applicable for cohesion soils. The final formula for the shear strength of a soil material can be described as

$$\tau_f = c + \sigma' \tan \phi \quad (58)$$

where

$\sigma'$  is the effective stress

$c$  is the cohesion

$\phi$  is the angle of friction

### Mohr's circle

#### Derivation of the formulas for $\tau$ and $\sigma_n$

Suppose an element subjected to stresses perpendicular to the surfaces according to Figure 44.

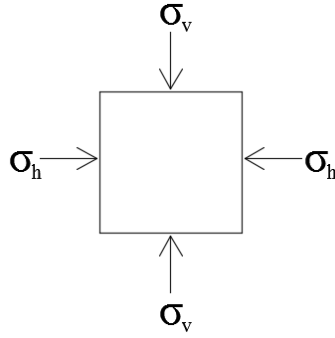


Figure 44 Body element

A triangular piece of the element is displayed in Figure 45. The equilibrium of forces are applied and this concludes that:

$$\sigma_n A - \sigma_h \sin \theta (A \sin \theta) - \sigma_v \cos \theta (A \cos \theta) = 0 \quad (59)$$

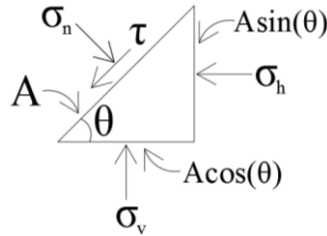


Figure 45 Element piece

Both sides are divided by the area, A, and the formula is reorganized to

$$\sigma_n = \sigma_h \sin^2 \theta + \sigma_v \cos^2 \theta \quad (60)$$

By the help of the two standard trigonometric relations

$$\sin^2 \theta = \frac{1 - \cos 2\theta}{2} \quad (61)$$

and

$$\cos^2 \theta = \frac{1 + \cos 2\theta}{2} \quad (62)$$

it is concluded that the normal stress can be described as

$$\sigma_n = \frac{(\sigma_v + \sigma_h)}{2} + \frac{(\sigma_v - \sigma_h)}{2} \cos 2\theta \quad (63)$$

The force equilibrium parallel to the surfaces of the triangular element in Figure 45 results in

$$\tau A + \sigma_h \cos \theta A \sin \theta - \sigma_v \sin \theta A \cos \theta = 0 \quad (64)$$

both sides are divided by A and the shear stress can be expressed as

$$\tau = \sigma_v \sin \theta \cos \theta - \sigma_h \cos \theta \sin \theta \quad (65)$$

The basic trigonometric formula

$$\sin \theta \cos \theta = \frac{\sin 2\theta}{2} \quad (66)$$

is employed, and the shear stress can be expressed in the simpler form

$$\tau = \frac{\sigma_v - \sigma_h}{2} \sin 2\theta \quad (67)$$

### Construction of the circle

Consider a diagram as in Figure 46. The first principal stress,  $\sigma_v$  and the second principal stress,  $\sigma_h$ , is then added to the horizontal axis in the diagram. The distance from the intersection between the horizontal and the vertical axis to the midpoint of the circle is equal to the first term in the formula for the normal stress,  $\sigma_n$ . The horizontal distance from the intersection between the circle and the angle vector that goes from the midpoint of the circle is equal to the second term in the same formula, concludes that the formula for the normal stress can be described as

$$\sigma'_n = \frac{(\sigma_v + \sigma_h)}{2} + \frac{(\sigma_v - \sigma_h)}{2} \cos 2\theta \quad (68)$$

which is previously stated.

Trigonometry in the same circle also concludes that the expression for the shear stress is valid, i.e.

$$\tau' = \frac{\sigma_v - \sigma_h}{2} \sin 2\theta \quad (69)$$

Eq. 64 and Eq 68 are illustrated in Figure 46 with the shear stress on the vertical axis and the normal stress on the horizontal axis.

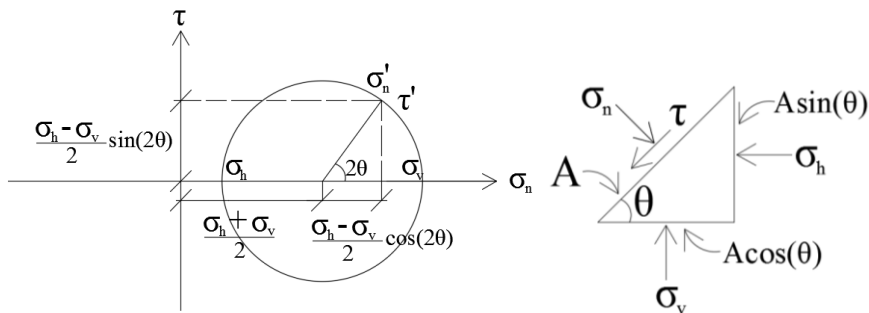


Figure 46 Mohr's circle

### Mohr-Coulomb failure criterion

Failure in soils occur when the shear stresses exceed the shear strength. By combining Mohr's circle and Coulombs criterion, both a graphic and a mathematical solution can be obtained for the failure stress.

By introducing the Coulombs failure criterion in the same diagram as Mohr's circle, Figure 47 is obtained.

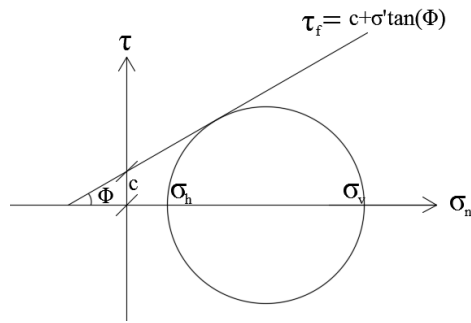


Figure 47 Mohr-Coulomb failure criterion

Failure in the soil occurs if the circle expands over the linear function for the Coulomb shear strength,  $\tau_f$ . The mathematical solution can be obtained by calculating where  $\tau_f$  tangent the surface of the circle. The failure stress can be expressed as (Labuz & Zang, 2012)

$$\sigma'_v = \sigma'_h \frac{1 + \sin \phi}{1 - \sin \phi} + 2c \frac{\cos \phi}{1 - \sin \phi} \quad (70)$$

In three dimensions the failure surface is a cone shaped hexagonal, as can be seen in Figure 48

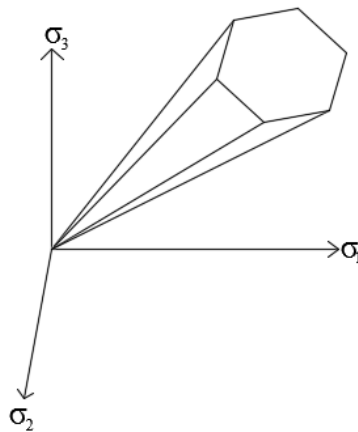


Figure 48 Mohr-Coulomb 3D failure surface

# Appendix

## B

### Application of the finite element method

By studying a linear elastic response within a spring system, the normal force  $N$  can in accordance with Hooke's law be written as:

$$N = k(u_2 - u_1) \quad (71)$$

Where  $k$  is the spring stiffness and  $u_i$  are the element displacements. If there's a spring exposed for two element forces,  $P_1$  and  $P_2$  and  $P_2 = N$ , i.e a normal force, the following can be written:

$$P_1 = k(u_1 - u_2) \quad (72)$$

$$P_2 = k(u_2 - u_1) \quad (73)$$

The equations can be written in a matrix form as:

$$\begin{bmatrix} k & -k \\ -k & k \end{bmatrix} \begin{bmatrix} u_1 \\ u_2 \end{bmatrix} = \begin{bmatrix} P_1 \\ P_2 \end{bmatrix} \quad (74)$$

or

$$\mathbf{K}^e \mathbf{a}^e = \mathbf{f}^e \quad (75)$$

where the terms for an element is  $\mathbf{K}^e = \begin{bmatrix} k & -k \\ -k & k \end{bmatrix}$ ,  $\mathbf{a}^e = \begin{bmatrix} u_1 \\ u_2 \end{bmatrix}$  and  $\mathbf{f}^e = \begin{bmatrix} P_1 \\ P_2 \end{bmatrix}$

When combining two spring elements in series, element 1 and 2 can be written as:

$$\begin{bmatrix} k_1 & -k_1 \\ -k_1 & k_1 \end{bmatrix} \begin{bmatrix} u_1^1 \\ u_2^1 \end{bmatrix} = \begin{bmatrix} P_1^1 \\ P_2^1 \end{bmatrix}, \text{ element 1} \quad (76)$$

$$\begin{bmatrix} k_2 & -k_2 \\ -k_2 & k_2 \end{bmatrix} \begin{bmatrix} u_1^2 \\ u_2^2 \end{bmatrix} = \begin{bmatrix} P_1^2 \\ P_2^2 \end{bmatrix}, \text{ element 2} \quad (77)$$

The notations above describe the elements independently. When combining the elements, one can see there are just three displacements in the global domain since:

$u_1^1 = u_1$ ,  $u_2^2 = u_3$  and the displacement in the connected nodal gives  $u_2^1 = u_1^2$

The notation can be expanded so a global version comprises the specific element stiffness matrix, the specific element force vector and the **global** nodal displacement vector. For the two-element-example above, the expanded element form can be written as:

$$\mathbf{K}_i^{ee} \mathbf{a} = \mathbf{f}_i^{ee}, \quad (78)$$

$$\begin{bmatrix} k_1 & -k_1 & 0 \\ -k_1 & k_1 & 0 \\ 0 & 0 & 0 \end{bmatrix} \begin{bmatrix} u_1 \\ u_2 \\ u_3 \end{bmatrix} = \begin{bmatrix} P_1^1 \\ P_2^1 \\ 0 \end{bmatrix}, \text{element 1} \quad (79)$$

$$\begin{bmatrix} 0 & 0 & 0 \\ 0 & k_2 & -k_2 \\ 0 & -k_2 & k_2 \end{bmatrix} \begin{bmatrix} u_1 \\ u_2 \\ u_3 \end{bmatrix} = \begin{bmatrix} 0 \\ P_1^2 \\ P_2^2 \end{bmatrix}, \text{element 2} \quad (80)$$

A force vector can be determined in the same way as for the displacement vector giving:

$P_1^1 = F_1$ ,  $P_2^2 = F_3$  and the force in the connected nodal gives  $F_2 = P_2^1 + P_1^2$

For the two-element example, the system of equation for the elements combined can be written as:

$$\begin{bmatrix} k_1 & -k_1 & 0 \\ -k_1 & k_1 + k_2 & -k_2 \\ 0 & -k_2 & k_2 \end{bmatrix} \begin{bmatrix} u_1 \\ u_2 \\ u_3 \end{bmatrix} = \begin{bmatrix} F_1 \\ F_2 \\ F_3 \end{bmatrix} \quad (81)$$

This way of constructing a system of equation is useful when dealing with many elements and can be written in a general form as:

$$\mathbf{K} \mathbf{a} = \mathbf{f} \quad (82)$$

where the global stiffness matrix  $\mathbf{K}$  combines all the expanded element stiffness matrices in its specified order.  $\mathbf{a}$  contains all the global displacements while  $\mathbf{f}$  contains the external forces applied in the global nodal points:

$$\mathbf{K} = \sum_{j=1}^N \mathbf{K}_j^{ee} \quad (83)$$

and

$$\mathbf{f} = \sum_{j=1}^N \mathbf{f}_j^{ee} \quad (84)$$

When handling soil, an analysis of three-dimensional stresses and strains are of importance.

For a three-dimensional stress case, the differential equations of equilibrium expressed in a compact matrix form is:

$$\tilde{\nabla}^T \boldsymbol{\sigma} + \mathbf{b} = 0 \quad (85)$$

where  $\tilde{\nabla}^T$  is the matrix differential operator,  $\boldsymbol{\sigma}$  the stress components and  $\mathbf{b}$  the body force such as:

$$\tilde{\nabla}^T = \begin{bmatrix} \frac{\partial}{\partial x} & 0 & 0 & \frac{\partial}{\partial y} & \frac{\partial}{\partial z} & 0 \\ 0 & \frac{\partial}{\partial y} & 0 & \frac{\partial}{\partial x} & 0 & \frac{\partial}{\partial z} \\ 0 & 0 & \frac{\partial}{\partial z} & 0 & \frac{\partial}{\partial x} & \frac{\partial}{\partial y} \end{bmatrix}; \boldsymbol{\sigma} = \begin{bmatrix} \sigma_{xx} \\ \sigma_{yy} \\ \sigma_{zz} \\ \sigma_{xy} \\ \sigma_{xz} \\ \sigma_{yz} \end{bmatrix}; \mathbf{b} = \begin{bmatrix} b_x \\ b_y \\ b_z \end{bmatrix} \quad (86)$$

The deformation of a three-dimensional body can be expressed via displacement components. The displacement vector  $\mathbf{u}$  collects the components. This gives the displacements of an arbitrary point  $(x, y, z)$  being a function of  $\mathbf{u} = \mathbf{u}(x, y, z)$  :

$$\mathbf{u} = \begin{bmatrix} u_x \\ u_y \\ u_z \end{bmatrix} \quad (87)$$

For a neighbouring point,  $(x + dx, y + dy, z + dz)$  the displacement is  $\mathbf{u} + d\mathbf{u}$ , with  $d\mathbf{u}$  being:

$$d\mathbf{u} = \begin{bmatrix} du_x \\ du_y \\ du_z \end{bmatrix} = \begin{bmatrix} \frac{\partial u_x}{\partial x} dx + \frac{\partial u_x}{\partial y} dy + \frac{\partial u_x}{\partial z} dz \\ \frac{\partial u_y}{\partial x} dx + \frac{\partial u_y}{\partial y} dy + \frac{\partial u_y}{\partial z} dz \\ \frac{\partial u_z}{\partial x} dx + \frac{\partial u_z}{\partial y} dy + \frac{\partial u_z}{\partial z} dz \end{bmatrix} \quad (88)$$

From the displacement, the normal strains could be described as:

$$\varepsilon_{xx} = \frac{\partial u_x}{\partial x}; \varepsilon_{yy} = \frac{\partial u_y}{\partial y}; \varepsilon_{zz} = \frac{\partial u_z}{\partial z}; \quad (89)$$

The traction vector  $\mathbf{t}$  is a vector which describes the stress  $[\text{N}/\text{m}^2]$  in an infinitely small surface area, related to a surface with the outer unit normal vector  $\mathbf{n}$ . For a surface where the infinitely small surface area  $d\mathbf{A} \rightarrow 0$ , the stress arising from the force vector  $d\mathbf{P}$  can be described as:

$$\mathbf{t} = \frac{d\mathbf{P}}{dA}, dA \rightarrow 0; \mathbf{t} = \begin{bmatrix} t_x \\ t_y \\ t_z \end{bmatrix} \quad (90)$$

On the boundary of a body, the traction vector must fulfil the boundary condition:

$$\begin{aligned} t_x &= \sigma_{xx}n_x + \sigma_{xy}n_y + \sigma_{xz}n_z \\ t_y &= \sigma_{yx}n_x + \sigma_{yy}n_y + \sigma_{yz}n_z \\ t_z &= \sigma_{zx}n_x + \sigma_{zy}n_y + \sigma_{zz}n_z \end{aligned} \quad (91)$$

When finding a general finite element formulation of three-dimensional elasticity, a good start is to determine the weak formulation of the differential equation of equilibrium. The weak form is a formulation where the equation is not required to hold absolutely, but gets weak solutions with respect to test functions. With the use of an arbitrary vector  $\mathbf{v}$ , one can begin the finding of a weak formulation of a three-dimensional-elasticity (Ottosen & Petersson, 1992) :

$$\mathbf{v} = \begin{bmatrix} v_x \\ v_y \\ v_z \end{bmatrix} \quad (92)$$

Combined with the non-transposed differential operator in (31):

$$\tilde{\mathbf{v}} = \begin{bmatrix} \frac{\partial v_x}{\partial x} \\ \frac{\partial v_y}{\partial y} \\ \frac{\partial v_z}{\partial z} \\ \frac{\partial v_x}{\partial y} + \frac{\partial v_y}{\partial x} \\ \frac{\partial v_x}{\partial z} + \frac{\partial v_z}{\partial x} \\ \frac{\partial v_y}{\partial z} + \frac{\partial v_z}{\partial y} \end{bmatrix} \quad (93)$$

With the use of recent equations:

$$\begin{aligned} (\tilde{\mathbf{v}})^T \boldsymbol{\sigma} = & \frac{\partial v_x}{\partial x} \sigma_{xx} + \frac{\partial v_y}{\partial y} \sigma_{yy} + \frac{\partial v_z}{\partial z} \sigma_{zz} + \left( \frac{\partial v_x}{\partial y} + \frac{\partial v_y}{\partial x} \right) \sigma_{xy} + \left( \frac{\partial v_x}{\partial z} + \frac{\partial v_z}{\partial x} \right) \sigma_{xz} \\ & + \left( \frac{\partial v_y}{\partial z} + \frac{\partial v_z}{\partial y} \right) \sigma_{yz} \end{aligned} \quad (94)$$

With this expression, the equations of equilibrium, eq. 85 can be expressed in a weak form. By multiplying each element in the arbitrary function  $\mathbf{v}$  with the equations of equilibrium and integrate over the body volume  $V$ , one obtain an expression of interest. Following is an example of the first out of three elements:

$$\int_V v_x \frac{\partial \sigma_{xx}}{\partial x} dV + \int_V v_x \frac{\partial \sigma_{xy}}{\partial y} dV + \int_V v_x \frac{\partial \sigma_{xz}}{\partial z} dV + \int_V v_x b_x dV = 0 \quad (95)$$

Integration by parts using Green-Gauss theorem gives:

$$\begin{aligned} \int_S v_x \sigma_{xx} n_x dS - \int_V \frac{\partial v_x}{\partial x} \sigma_{xx} dV + \int_S v_x \sigma_{xy} n_y dS - \int_V \frac{\partial v_x}{\partial y} \sigma_{xy} dV \\ + \int_S v_x \sigma_{xz} n_z dS - \int_V \frac{\partial v_x}{\partial z} \sigma_{xz} dV + \int_V v_x b_x dV = 0 \end{aligned} \quad (96)$$

Previously the traction vector  $\mathbf{t}$  was presented in eq.90. Since  $\mathbf{t}$  is related to the normal unit vector of a surface:

$$\sigma_{ii} \mathbf{n}_i = \mathbf{t}_i \quad (97)$$

This means eq.96 can be written as:

$$\int_S v_x t_x dS - \int_V \left( \frac{\partial v_x}{\partial x} \sigma_{xx} + \frac{\partial v_x}{\partial y} \sigma_{xy} + \frac{\partial v_x}{\partial z} \sigma_{xz} \right) dV + \int_V v_x b_x dV = 0 \quad (98)$$

Doing this for the rest of the elements in  $y$ - and  $z$ - direction, and using once again expression 94 one will obtain the weak formulation as:

$$\int_V (\tilde{\mathbf{v}})^T \boldsymbol{\sigma} dV = \int_S \mathbf{v}^T \mathbf{t} dS + \int_V \mathbf{v}^T \mathbf{b} dV \quad (99)$$

With the weak formulation of the equation of equilibrium, the finite element formulation (FE-formulation) of three-dimensional elasticity can be described. The assumption of elasticity should be introduced as late as possible in the stage of formulation the FE-formulation due to the fact the formulation should be as general as possible (Ottosen & Petersson, 1992).

According to them, the strategy to achieve that purpose is to introduce the assumption of the displacement vector  $\mathbf{u}$  and the use of the Galerkin method for choosing the arbitrary vector  $\mathbf{v}$  (expression 92). With the use of shape functions the displacement vector  $\mathbf{u}$  can be written as:

$$\mathbf{u} = \mathbf{N} \mathbf{a} \quad (100)$$

With  $\mathbf{N}$  being the element shape functions and  $\mathbf{a}$  the nodal displacement of the elements.

The arbitrary weight vector  $\mathbf{v}$  is chosen so it fulfills:

$$\mathbf{v} = \mathbf{N} \mathbf{c} \quad (101)$$

with  $\mathbf{c}$  being an arbitrary matrix. One could then express:

$$\tilde{\mathbf{v}} = \mathbf{B} \mathbf{c} \text{ with } \mathbf{B} = \tilde{\mathbf{v}} \mathbf{N} \quad (102)$$

Inserting 101 and 102 into the weak form, eq.99 , gives:

$$\mathbf{c}^T \left( \int_V \mathbf{B}^T \boldsymbol{\sigma} dV - \int_S \mathbf{N}^T \mathbf{t} dS - \int_V \mathbf{N}^T \mathbf{b} dV \right) = 0 \quad (103)$$

This gives:

$$\int_V \mathbf{B}^T \boldsymbol{\sigma} dV = \int_S \mathbf{N}^T \mathbf{t} dS + \int_V \mathbf{N}^T \mathbf{b} dV \quad (104)$$

In this stage the assumption that the material responds thermoelastically is introduced (Ottosen & Petersson, 1992). Kinematic relations suggests that the strains are the derivatives of the displacement as in eq. 89. This gives the strain to be expressed as:

$$\boldsymbol{\varepsilon} = \tilde{\mathbf{V}}\mathbf{u} \rightarrow \boldsymbol{\varepsilon} = \mathbf{B}\mathbf{a} \quad (105)$$

Since the constitutive model is:

$$\boldsymbol{\sigma} = \mathbf{D}\boldsymbol{\varepsilon} - \mathbf{D}\boldsymbol{\varepsilon}_0 \quad (106)$$

It could be rewritten as:

$$\boldsymbol{\sigma} = \mathbf{D}\mathbf{B}\mathbf{a} - \mathbf{D}\boldsymbol{\varepsilon}_0 \quad (107)$$

Inserted into eq. 104 and with the use of the definitions of the boundary conditions, the FE-formulation becomes:

$$\int_V \mathbf{B}^T \mathbf{D} \mathbf{B} dV \mathbf{a} = \int_{S_h} \mathbf{N}^T \mathbf{h} dS + \int_{S_g} \mathbf{N}^T \mathbf{t} dS + \int_V \mathbf{N}^T \mathbf{b} dV + \int_V \mathbf{B}^T \mathbf{D} \boldsymbol{\varepsilon}_0 dV \quad (108)$$

The FE-formulation written in the compact form:

$$\mathbf{K}\mathbf{a} = \mathbf{f}_b + \mathbf{f}_l + \mathbf{f}_0 \quad (109)$$